

# Galaxy and Mass Assembly: FUV, NUV, *ugrizYJHK* Petrosian, Kron and Sérsic photometry

David T. Hill,<sup>1\*</sup> Lee S. Kelvin,<sup>1</sup> Simon P. Driver,<sup>1</sup> Aaron S. G. Robotham,<sup>1</sup>  
Ewan Cameron,<sup>1,2</sup> Nicholas Cross,<sup>3</sup> Ellen Andrae,<sup>4</sup> Ivan K. Baldry,<sup>5</sup>  
Steven P. Bamford,<sup>6</sup> Joss Bland-Hawthorn,<sup>7</sup> Sarah Brough,<sup>8</sup> Christopher J. Conselice,<sup>6</sup>  
Simon Dye,<sup>9</sup> Andrew M. Hopkins,<sup>8</sup> Jochen Liske,<sup>10</sup> Jon Loveday,<sup>11</sup> Peder Norberg,<sup>3</sup>  
John A. Peacock,<sup>3</sup> Scott M. Croom,<sup>7</sup> Carlos S. Frenk,<sup>12</sup> Alister W. Graham,<sup>13</sup>  
D. Heath Jones,<sup>8</sup> Konrad Kuijken,<sup>14</sup> Barry F. Madore,<sup>15</sup> Robert C. Nichol,<sup>16</sup>  
Hannah R. Parkinson,<sup>3</sup> Steven Phillipps,<sup>17</sup> Kevin A. Pimbblet,<sup>18</sup> Cristina C. Popescu,<sup>19</sup>  
Matthew Prescott,<sup>5</sup> Mark Seibert,<sup>15</sup> Rob G. Sharp,<sup>8</sup> Will J. Sutherland,<sup>20</sup>  
Daniel Thomas,<sup>16</sup> Richard J. Tuffs<sup>4</sup> and Elco van Kampen<sup>10</sup>

<sup>1</sup>*School of Physics & Astronomy, University of St Andrews, North Haugh, St Andrews KY16 9SS (SUPA)*

<sup>2</sup>*Department of Physics, Swiss Federal Institute of Technology (ETH-Zürich), 8093 Zürich, Switzerland*

<sup>3</sup>*Institute for Astronomy, University of Edinburgh, Royal Observatory, Blackford Hill, Edinburgh EH9 3HJ (SUPA)*

<sup>4</sup>*Max Planck Institute for Nuclear Physics (MPIK), Saupfercheckweg 1, 69117 Heidelberg, Germany*

<sup>5</sup>*Astrophysics Research Institute, Liverpool John Moores University, Twelve Quays House, Egerton Wharf, Birkenhead CH41 1LD*

<sup>6</sup>*Centre for Astronomy and Particle Theory, University of Nottingham, University Park, Nottingham NG7 2RD*

<sup>7</sup>*Sydney Institute for Astronomy, School of Physics, University of Sydney, NSW 2006, Australia*

<sup>8</sup>*Anglo Australian Observatory, PO Box 296, Epping, NSW 1710, Australia*

<sup>9</sup>*School of Physics and Astronomy, Cardiff University, The Parade, Cardiff CF24 3AA*

<sup>10</sup>*European Southern Observatory, Karl-Schwarzschild-Str. 2, 85748 Garching, Germany*

<sup>11</sup>*Astronomy Centre, University of Sussex, Falmer, Brighton BN1 9QH*

<sup>12</sup>*Institute for Computational Cosmology, Department of Physics, Durham University, South Road, Durham DH1 3LE*

<sup>13</sup>*Centre for Astrophysics and Supercomputing, Swinburne University of Technology, Hawthorn, Victoria 3122, Australia*

<sup>14</sup>*Leiden University, PO Box 9500, 2300 RA Leiden, the Netherlands*

<sup>15</sup>*Observatories of the Carnegie Institution of Washington, 813 Santa Barbara Street, Pasadena, CA 91101, USA*

<sup>16</sup>*Institute of Cosmology and Gravitation (ICG), University of Portsmouth, Dennis Sciama Building, Burnaby Road, Portsmouth PO1 3FX*

<sup>17</sup>*Astrophysics Group, H.H. Wills Physics Laboratory, University of Bristol, Tyndall Avenue, Bristol BS8 1TL*

<sup>18</sup>*School of Physics, Monash University, Clayton, VIC 3800, Australia*

<sup>19</sup>*Jeremiah Horrocks Institute, University of Central Lancashire, Preston PR1 2HE*

<sup>20</sup>*Astronomy Unit, Queen Mary University London, Mile End Road, London E1 4NS*

Accepted 2010 October 27. Received 2010 September 1; in original form 2010 July 12

## ABSTRACT

In order to generate credible 0.1–2  $\mu\text{m}$  spectral energy distributions, the Galaxy and Mass Assembly (GAMA) project requires many gigabytes of imaging data from a number of instruments to be reprocessed into a standard format. In this paper, we discuss the software infrastructure we use, and create self-consistent *ugrizYJHK* photometry for all sources within the GAMA sample. Using UKIDSS and SDSS archive data, we outline the pre-processing necessary to standardize all images to a common zero-point, the steps taken to correct for the seeing bias across the data set and the creation of gigapixel-scale mosaics of the three  $4 \times 12 \text{ deg}^2$  GAMA regions in each filter. From these mosaics, we extract source catalogues for the GAMA regions using elliptical Kron and Petrosian matched apertures. We also calculate

\*E-mail: dth4@st-andrews.ac.uk

Sérsic magnitudes for all galaxies within the GAMA sample using `SIGMA`, a galaxy component modelling wrapper for `GALFIT 3`. We compare the resultant photometry directly and also calculate the  $r$ -band galaxy luminosity function for all photometric data sets to highlight the uncertainty introduced by the photometric method. We find that (1) changing the object detection threshold has a minor effect on the best-fitting Schechter parameters of the overall population ( $M^* \pm 0.055$  mag,  $\alpha \pm 0.014$ ,  $\phi^* \pm 0.0005 h^3 \text{Mpc}^{-3}$ ); (2) there is an offset between data sets that use Kron or Petrosian photometry, regardless of the filter; (3) the decision to use circular or elliptical apertures causes an offset in  $M^*$  of 0.20 mag; (4) the best-fitting Schechter parameters from total-magnitude photometric systems (such as SDSS `MODEL MAG` or Sérsic magnitudes) have a steeper faint-end slope than photometric systems based upon Kron or Petrosian measurements; and (5) our Universe's total luminosity density, when calculated using Kron or Petrosian  $r$ -band photometry, is underestimated by at least 15 per cent.

**Key words:** methods: data analysis – methods: observational – techniques: image processing – techniques: photometric – surveys – galaxies: fundamental parameters.

## 1 INTRODUCTION

When calculating any statistic, it is essential that the sample used to generate it is both numerous and without systematic bias. For a number of fundamental parameters in cosmology, for example, the galaxy stellar mass function or the total luminosity density, the data set used will be made up of a large sample of galaxies and contain a measure of the flux from each galaxy (e.g. Hill et al. 2010). Unfortunately, our ability to accurately calculate the flux of any galaxy is imprecise; at some distance from its centre, the luminosity of the galaxy will drop into the background noise and the quantification of the missing light beyond that point is problematic with no obviously correct procedure. Even using deep photometry ( $\mu_B > 29$  mag arcsec<sup>2</sup>), Caon, Capaccioli & Rampazzo (1990) did not reveal the presence of an elliptical galaxy light profile truncation.

A number of methods to calculate the flux from a galaxy have been proposed. They tend to be either simple and impractical, such as setting the aperture to be of a fixed constant size or limiting it using a detection threshold (ignoring the missing light issue completely), or complex and subject to bias, such as using the light distribution of the easily detected part of the object to calculate the size the aperture should be set to (Petrosian 1976; Kron 1980), which will return a different fraction of the total light emission, depending on whether the galaxy follows an exponential (Patterson 1940; Freeman 1970) or de Vaucouleurs (1948) light profile. Cross & Driver (2002) discuss the use of different missing-light estimators and their inherent selection effects. A third option is to attempt to fit a light profile, such as the aforementioned de Vaucouleur and exponential profiles (i.e. SDSS model magnitudes, Stoughton et al. 2002), or the more general Sérsic profile (Sérsic 1963; Graham & Driver 2005) to the available data and integrate that profile to infinity to calculate a total-magnitude for the galaxy. Graham et al. (2005) investigate the discrepancy between the Sérsic and SDSS Petrosian magnitudes for different light profiles, providing a simple correction for SDSS data.

Unfortunately, no standard, efficacious photometric formula is used in all surveys. If one looks at three of the largest photometric surveys, the 2MASS, SDSS and UKIDSS, one finds a variety of methods. The 2MASS survey data set contains Isophotal and Kron circularized, elliptical aperture magnitudes (elliptical apertures with a fixed minimum semiminor axis) and an elliptical Sérsic total magnitude. The SDSS uses two methods for their extended source

photometry: `PETROMAG`, which fits a circular Petrosian aperture to an object, and `MODEL MAG`, which chooses whether an exponential or de Vaucouleur profile is the more accurate fit and returns a magnitude determined by integrating the chosen profile to a specified number of effective radii (profiles are smoothly truncated between 7 and  $8R_e$  for a de Vaucouleur profile and between 3 and  $4R_e$  for an exponential profile). The `MODEL MAGS` used in this paper specify the profile type in the  $r$  band and use that profile in each passband. UKIDSS catalogues were designed to have multiple methods: again a circular Petrosian magnitude and a 2D Sérsic magnitude, calculated by fitting the best Sérsic profile to the source. The 2D Sérsic magnitude has not yet been implemented. As these surveys then formed the basis for photometric calibration of other studies, it is important to understand any biases that may be introduced by the photometric method.

The Galaxy and Mass Assembly (GAMA) survey (Driver et al. 2009) is a multiwavelength (151.6 nm to  $\sim 6$  m), spectroscopic survey of galaxies within three  $4 \times 12$  deg<sup>2</sup> regions of the equatorial sky centred around 9<sup>h</sup>, 12<sup>h</sup> and 14.5<sup>h</sup> (with aspirations to establish further blocks in the South Galactic Pole). Amongst other legacy goals, the survey team will create a complete, magnitude-limited sample of galaxies with redshift and colour information from the far-ultraviolet (FUV) to radio passbands, in order to accurately model the active galactic nucleus, stellar, dust and gas contents of each individual galaxy. This requires the combination of observations from many surveys, each with different instrument resolutions, observational conditions and detection technologies. As the luminous output of different stellar populations peaks in different parts of the electromagnetic spectrum, it is not always a simple task to match an extended source across surveys. The SDSS, which covers only a relatively modest wavelength range (300–900 nm), detects objects using a combination of all filters, defines apertures using the  $r$  band and then applies them to *ugiz* observations to negate this problem. This ensures a consistent deblending outcome and accurate colours. The UKIDSS extraction pipeline generates independent detection lists separately in each frame (i.e. for every filter) and merges these lists together for frames that cover the same region of sky (a frame set). Sources are then defined as detections within a certain tolerance. This process is detailed in Hambly et al. (2008). Unfortunately, it is susceptible to differing deblending outcomes that may produce less-reliable colours. As a key focus of the GAMA survey is the production of optimal spectral energy distributions (SEDs), it is necessary for us to internally standardize the

photometry, so that is immune to aperture bias from  $u - K$ . The pipeline outlined in this paper is the result of these efforts.

Imaging data are taken from UKIDSS DR4/SDSS DR6 observations. The outline of this paper is as follows. In Section 2, we briefly outline the surveys that acquired the data we use in this work. In Section 3, we describe how we standardized our data and formed image mosaics for each filter/region combination. Section 4 discusses the photometric methods we use and in Sections 5 and 6, we discuss the source catalogues produced following source extraction on these mosaics. We define the photometry we are using as the GAMA standard in Section 7. Finally, in order to quantify the systematic bias introduced by the choice of the photometric method, we present  $r$ -band luminosity functions, calculated using a series of different photometric methods, in Section 8. Throughout we adopt an  $h = 1$ ,  $\Omega_M = 0.3$  and  $\Omega_\Lambda = 0.7$  cosmological model. All magnitudes are quoted in the AB system, unless otherwise stated. Execution speeds provided are from a run of the pipeline on a 16-processor server built in 2009. As other processes were running simultaneously, the processing speed will vary and these parameters should only be taken as approximate time-scales.

## 2 SURVEY DATA

### 2.1 GAMA

The GAMA project (Driver et al. 2009) aims to study galaxy formation and evolution using a range of cutting-edge instruments (AAT, VST, VISTA, ASKAP, HERSCHEL WISE, GALEX and GMRT), creating a data base of  $\sim 350\,000$  galaxies observed from UV to radio wavelengths. The first stage of the GAMA project, GAMA I, covers  $144\text{ deg}^2$  of the equatorial sky, in three separate  $4 \times 12\text{ deg}^2$  regions centred at  $9^{\text{h}} + 1^{\text{d}}$  (GAMA9),  $12^{\text{h}} + 0^{\text{d}}$  (GAMA12) and  $14^{\text{h}} 30^{\text{m}} + 0^{\text{d}}$  (GAMA15). These areas have complete SDSS coverage and we are in the process of obtaining complete UKIDSS-LAS coverage (Fig. 1). Between 2008 and 2010, the GAMA project was allocated 66 nights on the AAT to use the AAOmega spectrograph in order to carry out the GAMA I spectroscopic campaign.

A complete description of the input catalogue for the spectroscopic campaign can be found in Baldry et al. (2010). To summarize: the aim is to provide spectroscopy of all galaxies in the GAMA I regions brighter than  $r_{\text{petro,SDSS}} = 19.4\text{ mag}$ ,  $z_{\text{model,SDSS}} = 18.2\text{ mag}$

and  $K_{\text{kron,AB}} = 17.5\text{ mag}$ , with the sample extended to  $r_{\text{petro,SDSS}} < 19.8\text{ mag}$  in the GAMA12 region. Where a galaxy would not be selected by its  $r$  magnitude, but would be selected using the  $K$ - or  $z$ -magnitude cut, the galaxy must also have  $r_{\text{petro,SDSS}} < 20.5\text{ mag}$ . This ensures that the galaxy is credible and the likelihood of obtaining a redshift is reasonable. In order to guarantee a complete sample of galaxies, including compact objects, the GAMA input catalogue utilizes a star-galaxy selection algorithm that includes optical ( $r_{\text{psf}} - r_{\text{model}}$ ,  $g - i$ ) and infrared (IR) colour selections ( $J - K$ ). The latter uses colours taken from sources extracted using this pipeline.

The 2008 and 2009 observations make up a sample of 100 051 reliable redshifts, of which 82 696 come from the AAOmega spectrograph. The tiling strategy used to allocate objects to AAOmega fibres is detailed in Robotham et al. (2010). A breakdown of redshift completeness by luminosity and colour selection of the year 2 observations is shown in table 5 of Baldry et al., and in table 3 of the same paper, there is a list of spectra used from external surveys.

### 2.2 Sloan Digital Sky Survey

The SDSS (York et al. 2000) is the largest combined photometric and spectroscopic survey ever undertaken and contains spectra of 930 000 galaxies spread over  $8423\text{ deg}^2$  of sky, with imaging in five filters with effective wavelengths between 300 and 1000 nm (*ugriz*). SDSS data have been publicly released in a series of seven data releases. Abazajian et al. (2004) state that SDSS imaging is 95 per cent complete to  $u = 22.0\text{ mag}$ ,  $g = 22.2\text{ mag}$ ,  $r = 22.2\text{ mag}$ ,  $i = 21.3\text{ mag}$  and  $z = 20.5\text{ mag}$  (all depths measured for point sources in typical seeing using the SDSS photometric system, which is comparable in all bands to the AB system  $\pm 0.05\text{ mag}$ ).

Images are taken using an imaging array of  $30\,2048 \times 2048$  Tektronix CCDs with a pixel size of 0.396 arcsec, but only on nights where the seeing is  $< 1.5\text{ arcsec}$  and there is less than 1 per cent uncertainty in the zero-point. When such conditions are not reached, spectroscopy is attempted instead. SDSS catalogues can be accessed through the SDSS Catalog Archive Server (CAS) and imaging data through the Data Archive Server (DAS).

Astrometry for the SDSS-DR6 (Pier et al. 2003) is undertaken by comparing  $r$ -band observations to the USNO CCD Astrograph Catalog (UCAC, Zacharias et al. 2000), where it had coverage at

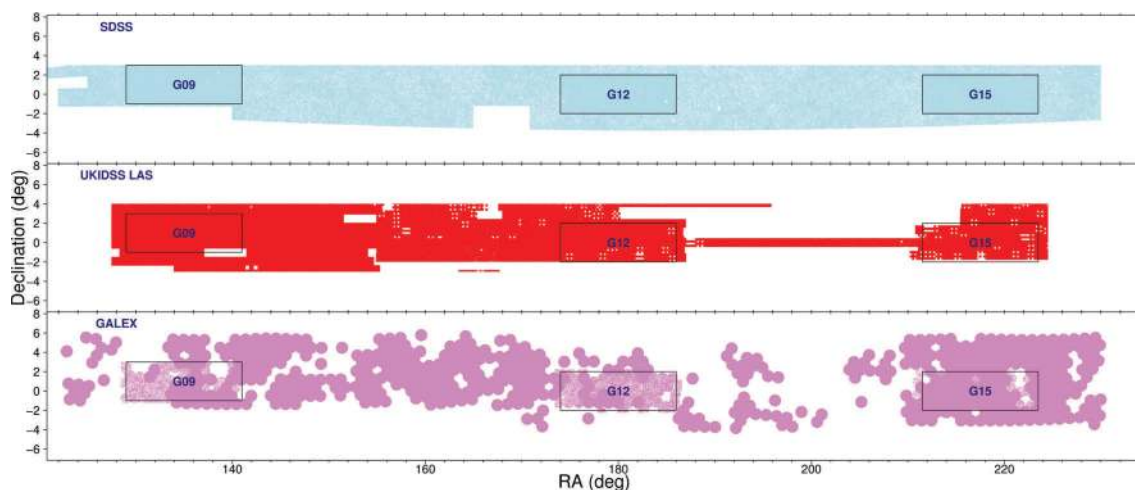


**Figure 1.** Coverage of the equatorial region of sky that contains the GAMA regions by SDSS DR6 (blue), UKIDSS LAS (red) and GALEX (violet) imaging. The three rectangular boxes contain the regions of sky surveyed by the GAMA.

the time of release, or Tycho-2 (Høg et al. 2000), when the UCAC did not have coverage. For sources brighter than  $r = 20$  mag, the astrometric accuracy when compared to the UCAC is 45 mas and when compared to Tycho-2 is 75 mas. In both cases, there is a further 30-mas systematic error and a relative error between filters (i.e. in *ugiz*) of 25–35 mas.

The GAMA input catalogue is defined using data from the SDSS DR6 (Adelman-McCarthy et al. 2008). The GAMA regions fall within the SDSS DR6 area of coverage, in SDSS stripes 9–12.

### 2.3 UKIDSS

UKIDSS (Lawrence et al. 2007) is a 7-yr near-IR (NIR) survey programme that will cover several thousand degrees of sky. The programme utilizes the Wide Field Camera (WFCAM) on the 3.8-m United Kingdom Infra-Red Telescope (UKIRT). The UKIDSS programme consists of five separate surveys, each probing to a different depth and for a different scientific purpose. One of these surveys, the UKIDSS Large Area Survey (LAS), will cover 4000 deg<sup>2</sup> and will overlap with the SDSS stripes 9–16, 26–33 and part of stripe 82. As the GAMA survey regions are within SDSS stripes 9–12, the LAS survey will provide high-density NIR photometric coverage over the entire GAMA area. The UKIDSS-LAS survey observes to a far greater depth ( $K_{\text{LAS}} = 18.2$  mag using the Vega magnitude system) than the previous Two-Micron All-Sky Survey (2MASS,  $K_{2\text{MASS}} = 15.50$  mag using the Vega magnitude system).

When complete, the LAS has target depths of  $K = 18.2$  mag,  $H = 18.6$  mag,  $J = 19.9$  mag (after two passes; this paper uses only the first  $J$  pass, which is complete to 19.5 mag) and  $Y = 20.3$  mag (all depths measured use the Vega system for a point source with  $5\sigma$  detection within a 2-arcsec aperture). Currently, observations have been conducted in the equatorial regions and will soon cover large swathes of the Northern Sky. It is designed to have a seeing full width at half-maximum (FWHM) of  $<1.2$  arcsec, photometric rms uncertainty of  $<\pm 0.02$  mag and astrometric rms of  $<\pm 0.1$  arcsec. Each position on sky will be viewed for 40 s per pass. All survey data for this paper are taken from the fourth data release (DR4).

The WFCAM Science Archive (WSA, Hambly et al. 2008) is the storage facility for post-pipeline, calibrated UKIDSS data. It provides users with access to fits images and CASU-generated object catalogues for all five UKIDSS surveys. We do not use the CASU-generated catalogues for a few reasons. First, the CASU catalogues for early UKIDSS data releases suffer from a fault where deblended objects are significantly brighter than their parent object, in some cases by several magnitudes (Smith, Loveday & Cross 2009; Hill et al. 2010). Secondly, the CASU catalogues only contain circular aperture fluxes. Thirdly, CASU decisions (e.g. deblending and aperture sizes) are not consistent between filters. For instance, the aperture radius and centre used to calculate  $K_{\text{PETROMAG}}$  of a source is not necessarily the same as the aperture radius and centre used to calculate  $Y_{\text{PETROMAG}}$  or  $H_{\text{PETROMAG}}$ . We require accurate extended-aperture colours; the CASU catalogues do not provide this.

## 3 CONSTRUCTION OF THE MOSAICS FROM SDSS AND UKIDSS IMAGING

One of GAMA’s priorities is the accurate measurement of SEDs from as broad a wavelength range as possible. This is non-trivial when combining data from multiple surveys. While each survey may be internally consistent with data collected contemporaneously, conditions between surveys can vary. In particular, seeing and zero-point parameters may greatly differ between frames. When

matching between surveys, one may find an object in the centre of the frame in one survey split across two frames in another survey. There may also be variation in the angular scale of a pixel between different instruments and even when two instruments have the same pixel size; a shift of half of a pixel between two frames can cause significant difficulties in calculating colours for small, low surface brightness objects. Furthermore, in order to use `SEXTRACTOR` in dual frame mode, the source-detection and the observation frame pixels must be calibrated to the same world coordinate system. In the GAMA survey, we have attempted to circumvent these difficulties by creating gigapixel-scale mosaics with a common zero-point and consistent WCS calibration. The construction process is outlined in this section.

To generate our image mosaics, we use the `TerapiX SWARP` (Bertin et al. 2002) utility. This is a mosaic-generation tool and how we utilize it is described in Section 3.4. Before we can use this software, however, it is necessary for us to normalize the contributing SDSS and UKIDSS data to take into account differences in sky conditions and exposure times between observations. For every file, we must identify its current zero-point (see the distribution in Fig. 2) and

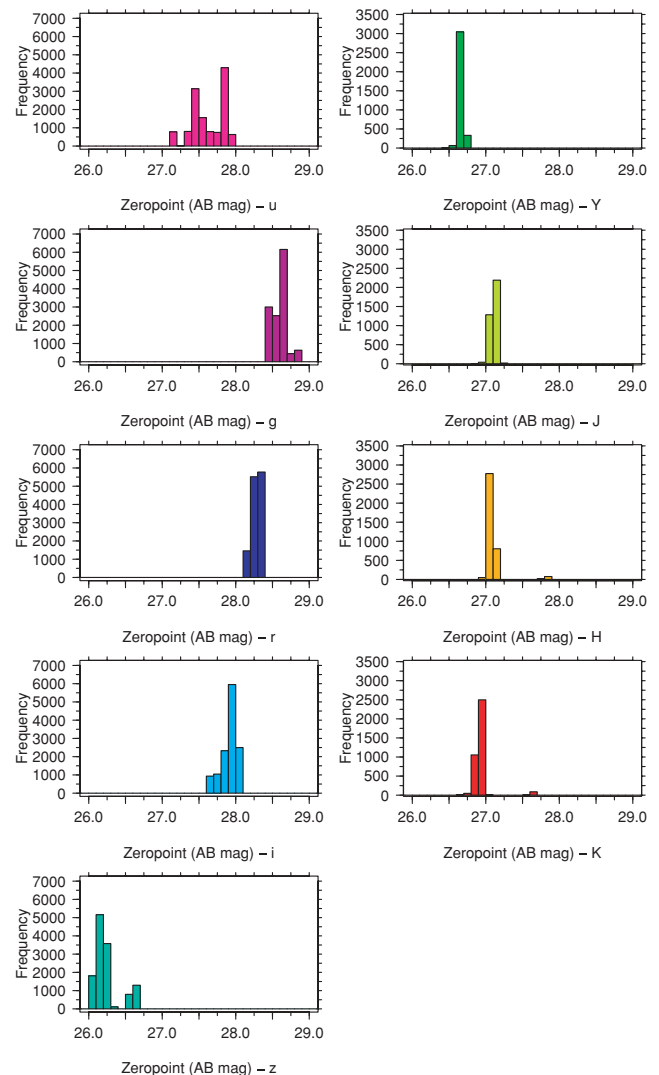


**Figure 2.** A histogram of the calculated total zero-points for the fields used to create our master region mosaics.

transform it to a defined standard. This process is described in Sections 3.1 and 3.2.

### 3.1 UKIDSS: acquisition of data and renormalization to a common zero-point

UKIDSS imaging is stored within the WFCAM Science Archive (WSA). We downloaded 862 *Y*-, 883 *J*-, 931 *H*- and 928 *K*-band compressed UKIDSS-LAS fits files that contained images of sky from the GAMA regions. These files were decompressed using the `IMCOPY` utility. The files for each band are stored and treated separately.

A specially designed pipeline accesses each file, reads the `MAGZPT` ( $ZP_{\text{mag}}$ ), `EXP_TIME` ( $t$ ), `airmass` [ $0.5 * (\text{AMSTART} + \text{AMEND}) = \sec\chi_{\text{mean}}$ ] and `EXTINCT` (`Ext`) keywords from the fits header and creates a total AB magnitude zero-point for the file using equation (1):

$$ZP_{\text{total}} = ZP_{\text{mag}} - 2.5 \log\left(\frac{1}{t}\right) - \text{Ext} \times (\sec\chi_{\text{mean}} - 1) + \text{ABV}_X, \quad (1)$$

where  $\text{ABV}_X$  is the AB magnitude of Vega in the  $X$  band (Table 1).

To correct each frame to a standard zero-point (30), the value of each pixel is multiplied by a factor, calculated using equation (2). Whilst we show the distribution of frame zero-points in Fig. 2 in bins of 0.1 mag, we use the actual zero-point of each frame to calculate the total AB magnitude zero-point. This has a far smaller variation (e.g. 0.02 mag in photometric conditions in the *JHK* filters; Warren et al. 2007).

$$\text{pixelmodifier} = 10^{-0.4(ZP_{\text{total}} - 30)}. \quad (2)$$

A new file is created to store the corrected pixel table and the `MAGZPT` fits header parameter is updated. The `SKYLEVEL` and `SKYNOISE` parameters are then scaled using the same multiplying factor. This process takes 3 s per file.

**Table 1.** Conversion to AB magnitudes. The SDSS photometric system is roughly equivalent to the AB magnitude system, with only small offsets in the  $u$  and  $z$  passbands. UKIDSS photometry is calculated on the Vega magnitude system and our conversions are from Hewett et al. (2006). Whilst we convert UKIDSS data using a high-precision parameter, it should be noted that the conversion uncertainty is only known to  $\sim \pm 0.02$  mag (Cohen, Wheaton & Megeath 2003).

Band	AB offset (mag)
<i>u</i>	-0.04
<i>g</i>	0
<i>r</i>	0
<i>i</i>	0
<i>z</i>	+0.02
<i>Y</i>	0.634
<i>J</i>	0.938
<i>H</i>	1.379
<i>K</i>	1.900

### 3.2 SDSS: acquisition of data and renormalization to a common zero-point

The `tsField` and `fpC` files for the 12757 SDSS fields that cover the GAMA regions were downloaded from the SDSS data archive server (`das.sdss.org`) for all five passbands. Again, the files for each passband are stored and treated separately.

We use a specially designed pipeline that brings in the ‘`aa`’ (zero-point), ‘`kk`’ (extinction coefficient) and ‘`airmass`’ keywords from a field’s `tsField` file, and the `EXPTIME` ( $t$ ) keyword from the same field’s `fpC` file. Combining these parameters using equation (3), we calculate the current total AB magnitude zero-point of the field ( $ZP_{\text{total}}$ ):

$$ZP_{\text{total}} = -aa - 2.5 \log(1/t) - kk \times \text{airmass} + \text{sAo}, \quad (3)$$

where ‘`sAo`’ is the offset between the SDSS magnitude system and the actual AB magnitude system ( $-0.04$  mag for  $u$ ,  $0.02$  mag for  $z$ , otherwise 0). The SDSS photometric zero-point uncertainty is estimated to be no larger than 0.03 mag in any band (Ivezić et al. 2004). We calculate the multiplier required to transform every pixel in the field (again using equation 2) to a standard zero-point (30). As every pixel must be modified by the same factor, we utilize the `FCARITH` program (part of the `FTOOLS` package) to multiply the entire image by `pixelmodifier`. `FCARITH` can normalize an SDSS image every 1.25 s.

### 3.3 Correction of seeing bias

As observations were taken in different conditions, there is an intrinsic seeing bias between different input images and between different filters (Fig. 3). This could cause inaccuracies in photometric colour measurements that use apertures defined in one filter to derive magnitudes in a second filter. To rectify this problem, it is necessary for us to degrade the better quality images to a lower seeing. However, if we degrade all images to our lowest quality seeing (3.12 arcsec), we should lose the ability to resolve the smallest galaxies in our sample. Therefore, we elect to degrade our normalized images to 2-arcsec seeing. The fraction of images with seeing worse than 2 arcsec is 4.4, 2.7, 2.5, 2.1, 1.7, 0, 0, 1.3 and 0.9 per cent in  $u$ ,  $g$ ,  $r$ ,  $i$ ,  $z$ ,  $Y$ ,  $J$ ,  $H$  and  $K$ , respectively. Images with worse seeing than 2 arcsec are included in our degraded seeing mosaics. We do not attempt to modify their seeing. Although each survey uses a different method of calculating the seeing within their data [the SDSS uses a double Gaussian to model the point spread function (PSF), the UKIDSS uses the average FWHM of the stellar sources within the image], we assume that the seeing provided for every frame is correct.

To achieve a final PSF FWHM of 2 arcsec ( $\sigma_{\text{final}}$ ), we assume that the seeing within an image follows a perfect Gaussian distribution,  $\sigma_{\text{initial}}$ . Theoretically, a Gaussian distribution can be generated from the convolution of two Gaussian distributions. The `FGAUSS` utility (also part of the `FTOOLS` package) can be used to convolve an input image with a circular Gaussian with a definable standard deviation ( $\sigma_{\text{req}}$ ), calculated using equation (4):

$$\sigma_{\text{req}} = \sqrt{\sigma_{\text{final}}^2 - \sigma_{\text{initial}}^2}. \quad (4)$$

As each UKIDSS frame has a different seeing value, it is necessary to break each fits file into its four constituent images. This is not necessary for SDSS images (which are stored in separate files). However, it is necessary to retrieve the SDSS image seeing from the image’s `tsField` file. The SDSS image seeing is stored in the `psf_width` column of the `tsField` file. Where an image has a seeing better than our specified value, we use the `FGAUSS` utility to convolve

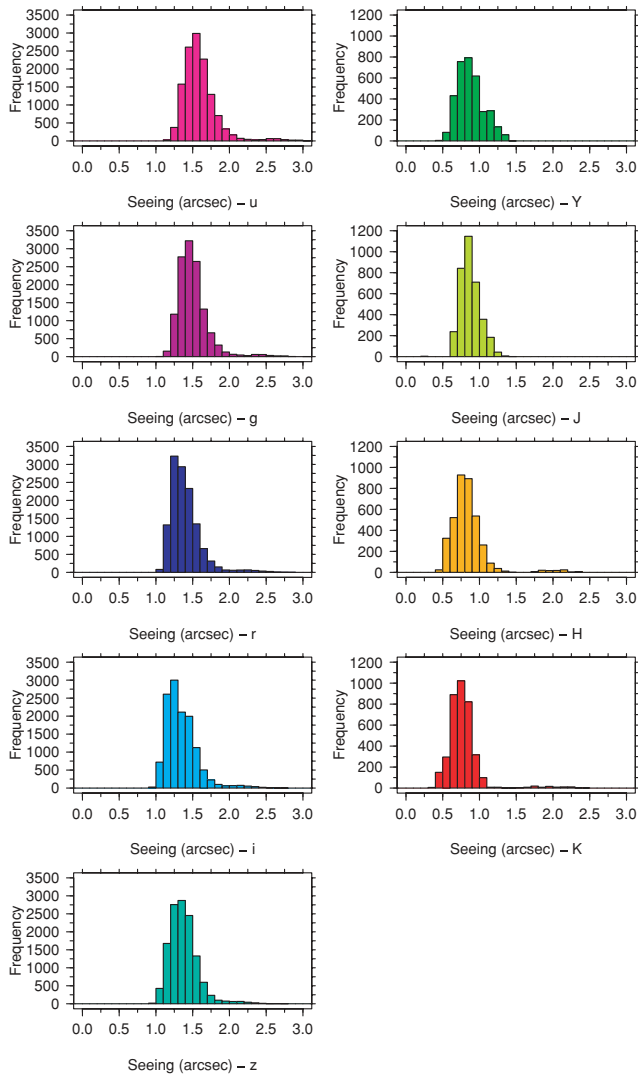


**Figure 3.** A histogram of the calculated seeing of the fields used to create our master region mosaics.

our image down to our specified value. Where an image has a seeing worse than our specified value, we copy it without modification using the `IMCOPY` utility. Both utilities produce a set of UKIDSS files containing two HDUs: the original instrument header HDU and a single image HDU with seeing greater than or equal to our specified seeing. The output SDSS files contain just a single image HDU. This process takes approximately 2 s per frame.

### 3.4 Creation of master region images

The `SWARP` utility is a multithread capable co-addition and image-warping tool that is part of the `Terapix` pipeline (Bertin et al. 2002). We use `SWARP` to generate complete images of the GAMA regions from the normalized LAS/SDSS fits files. It is vital that the pixel size and area of coverage are the same for each filter, as `SEXTRACTOR`'s dual-image mode requires perfectly matched frames. We define a pixel scale of  $0.4 \times 0.4$  arcsec and generate  $117\,000 \times 45\,000$  pixel files centred around  $09^{\text{h}}00^{\text{m}}00^{\text{s}}.0, +01^{\text{d}}00^{\text{m}}00^{\text{s}}.0$  (GAMA 9),  $12^{\text{h}}00^{\text{m}}00^{\text{s}}.0, +00^{\text{d}}00^{\text{m}}00^{\text{s}}.0$  (GAMA 12) and  $14^{\text{h}}30^{\text{m}}00^{\text{s}}.0, +00^{\text{d}}00^{\text{m}}00^{\text{s}}.0$  (GAMA 15). `SWARP` is set to resample input frames using the default `LANCZOS3` algo-

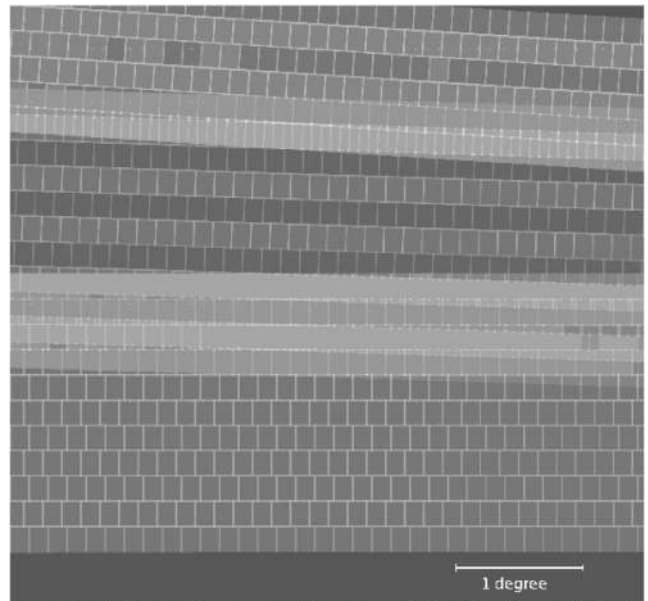


**Figure 4.** The *r*-band weight map of the  $45000 \times 45000$  pixel subset region ( $5 \times 5 \text{ deg}^2$ ; defined in Section 5). Joins and overlap between frames are apparent (light grey). The mosaic does not have imaging of the top right-hand corner or the bottom section (dark grey). These areas lie outside the region of interest as the mosaics are slightly larger in Dec. than the GAMA regions themselves.

rithm, which the `Terapix` team found was the optimal option when working with images from the `Megacam` instrument (Bertin et al. 2002).

`SWARP` produces mosaics that use the TAN WCS projection system. As UKIDSS images are stored in the ZPN projection system, `SWARP` internally converts the frames to the TAN projection system. There is also an astrometric distortion present in the UKIDSS images that `SWARP` corrects using the `pv2_3` and `pv2_1` fits header parameters.<sup>1</sup>

`SWARP` is set to subtract the background from the image, using a background mesh of  $256 \times 256$  pixels ( $102 \times 102$  arcsec) and a back filter size of  $3 \times 3$  to calculate the background map. The background calculation follows the same algorithm as `SEXTRACTOR` (Bertin & Arnouts 1996). To summarize: it is a bicubic-spline interpolation between the meshes, with a median filter applied to remove bright stars and artefacts.

Every mosaic contains pixels that are covered by multiple input frames. `SWARP` is set to use the median pixel value when a number of images overlap. The effects of outlying pixel values, due to cosmic rays, bad pixels or CCD edges, should therefore be reduced. `SWARP` generates a weight map (Fig. 4) that contains the flux variance in every pixel, calibrated using the background map described above. As the flux variance is affected by overlapping coverage, it is possible to see the survey footprint in the weight map. The weight map can be used within `SEXTRACTOR` to compensate for variations in noise. We do not use it when calculating our photometry for two reasons. First, there is overlap between SDSS fpC frames. This overlap is not from observations, but from the method used to cut the long SDSS stripes into sections. `SWARP` would not account for this and

<sup>1</sup>An analysis of the astrometric distortion can be found in the CASU document VDF-TRE-IOA-00009-0002, presently available at <http://www.ast.cam.ac.uk/vdfs/docs/reports/astrom/index.html>

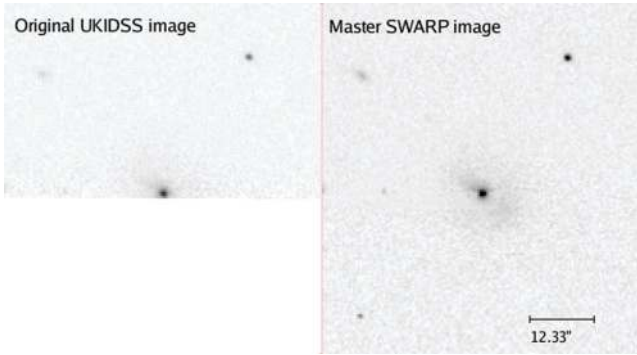


**Figure 5.** A comparison between the original normalized image and the  $K$ -band mosaic image of a galaxy on the bottom edge of an input UKIDSS frame. The bottom section of the galaxy is not part of this image and it has been stitched together on the mosaic using SWARP.

the weighting of the overlap regions on the optical mosaics would be calculated incorrectly. Secondly, using the weight maps would alter the effect of mosaic surface brightness limit variations upon our output catalogues. As we intend to model surface brightness effects later, we elect to use an unweighted photometric catalogue.

A small number of objects will be split between input frames. SWARP can reconstruct them, with only small defects due to CCD edges. One such example is shown in Fig. 5. We create both seeing-corrected and uncorrected mosaics for each passband and region combination. Each file is 20 Gb in size. In total, the mosaics require just over 1 Terabyte of storage space. Each mosaic takes approximately 4 h to create.

## 4 PHOTOMETRY

A major problem with constructing multiwavelength catalogues is that the definition of what constitutes an object can change across the wavelength range (see Appendix A, particularly Fig. A1). This can be due to internal structure, such as dust lanes or star-forming regions, becoming brighter or fainter in different passbands, causing the extraction software to deblend an object into a number of smaller parts in one filter but not in another. This can lead to large errors in the resulting colours. We cannot be certain that the SDSS object extraction process would produce the same results as the extraction process we use to create our UKIDSS object catalogues. Seeing, deblending and aperture sizes will differ, compromising colours. To create a consistent multiwavelength sample, the photometry needs to be recalculated consistently across all nine filters. At the same time, we can move from the circular apertures of the SDSS and UKIDSS to full elliptical apertures, as well as investigate a variety of photometric methods. To generate our source catalogues, we use the SExtractor software (Bertin & Arnouts 1996). This is an object extraction utility and its use is described in Section 4.5.

In this paper, we implement four different methods to define our object positions and apertures. We produce three SExtractor catalogues (Bertin & Arnouts 1996) and one Sérsic catalogue (based upon GALFIT 3, Peng et al. 2007), in addition to the original SDSS data set. The generation of the three new SExtractor catalogues is detailed in Section 4.5. Each of the new SExtractor catalogues contains magnitudes calculated using two different elliptical, extended source apertures: the Kron and the Petrosian magnitude systems. They are briefly described in Sections 4.1–4.3. We also use a specially designed pipeline (SIGMA GAMA, Kelvin et al. 2010, based upon GALFIT 3) to calculate a total magnitude for each galaxy via

its best-fitting Sérsic profile. This aperture system, and the process used to generate it, is described in Sections 4.4 and 4.6.

It is not obvious which photometric method will produce the optimal solution. Whilst the Sérsic photometric method solves the missing light problem, it requires higher quality data to calculate the set of parameters that best model the galactic light profile. The Kron and Petrosian magnitude systems will work with lower quality data, but may underestimate the flux produced by a galaxy. In this section, we describe the photometric systems that we have used. Later, in Sections 6 and 8, we will examine the different results produced by the choice of the photometric system.

### 4.1 Self-defined Kron and Petrosian apertures

We construct an *independent* catalogue for each filter, containing elliptical Kron and Petrosian apertures. These independent catalogues are then matched across all nine wavebands using STILTS (see Section 4.7 and Taylor 2006). The apertures will therefore vary in size, potentially giving inconsistent colours, and as deblending decisions will also change, inconsistent matching between catalogues may occur. However, as the apertures are defined from the image they are used on, there can be no problem with magnitudes being calculated for objects that do not exist or with missing objects that are not visible in the  $r$  band.

The self-defined catalogues are generated from the basic mosaics, where no attempt to define a common seeing for the mosaic has been made. This method should generate the optimal list of sources in each band; however, as the precise definition of the source will vary with wavelength, the colours generated using this method will be inaccurate and subject to aperture bias. As the mosaic has variations in seeing, the PSF will also vary across the image.

### 4.2 $r$ -band-defined Kron and Petrosian apertures

We use SExtractor to define a sample of sources in the  $r$ -band image and then use the  $r$ -band position and aperture information to calculate their luminosity within each filter (using the SExtractor dual image mode). As the aperture definitions do not vary between wavebands, this method gives internally consistent colours and as the list itself does not change, source matching between filters is unnecessary. However, where an object has changed in size (see Appendix A), does not exist (e.g. an artefact in the  $r$ -band sample) or when the  $r$ -band aperture definition incorrectly includes multiple objects, the output colours may be compromised. Any object that is too faint to be visible within the  $r$ -band mosaic will also not be detected using this method. However, such objects will be fainter than the GAMA sample’s selection criteria and would not be included within our sample. The  $r$ -band-defined catalogues are generated from our seeing-degraded mosaics. They provide us with an optically defined source sample.

This method is analogous to the SDSS source catalogues, which define their apertures using the  $r$ -passband data (unless the object is not detected in  $r$ , in which case a different filter is chosen). However, the GAMA photometric pipeline has a broader wavelength range, as it now includes NIR measurements from the same aperture definition. Furthermore, the SDSS Petrosian magnitudes have not been seeing-standardized. While all data are taken at the same time, the diffraction limit is wavelength-dependent and different fractions of light will be missed, despite the use of a fixed aperture. SDSS model magnitudes do account for the effects of the PSF.

### 4.3 *K*-band-defined Kron and Petrosian apertures

This method works in the same way as the previous method, but uses the *K*-band image as the detection frame rather than the *r*-band image. We are limited in the total area, as the *K*-band coverage is currently incomplete. However, for samples that require complete colour coverage in all nine filters, this is not a problem. As with *r*-band-defined catalogues, the *K*-band-defined catalogues are generated from the seeing-corrected mosaics. They provide us with a NIR-defined source sample. The *K*-band-defined Kron magnitudes were used in the GAMA input catalogue (Baldry et al. 2010) to calculate the star–galaxy separation  $J - K$  colour and the *K*-band target selection.

### 4.4 Sérsic magnitudes

We use the SIGMA modelling wrapper (see Section 4.6 and Kelvin et al. 2010 for more details), which in turn uses the galaxy-fitting software GALFIT 3.0 (Peng et al. 2007) to fit a single-Sérsic component to each object independently in nine filters (*ugrizYJHK*) and recover their Sérsic magnitudes, indices, effective radii, position angles and ellipticities. Source positions are initially taken from the GAMA input catalogue, as defined in Baldry et al. (2010). All Sérsic magnitudes are self-defined; as each band is modelled independently of the others, the aperture definition will vary and colour may therefore be compromised.

Single-Sérsic fitting is comparable to the SDSS model magnitudes. SIGMA therefore should recover total fluxes for objects that have a Sérsic index in the range  $0.3 < n < 20$ , where model magnitudes force a fit to either an exponential ( $n = 1$ ) or deVaucouleurs ( $n = 4$ ) profile. The systematic magnitude errors that arise when model magnitudes are fitted to galaxies that do not follow an exponential or deVaucouleurs profile (Graham 2001; Brown et al. 2003) do not occur in SIGMA. The SDSS team developed a composite magnitude system, CMODEL, which calculates a magnitude from the combination of the  $n = 1$  and  $n = 4$  systems, in order to circumvent this issue (Abazajian et al. 2004). We compare our Sérsic magnitudes to their results later. Sérsic magnitudes do not suffer from the missing-flux issue that affects Kron and Petrosian apertures. Petrosian magnitudes may underestimate a galaxy’s luminosity by 0.2 mag (Strauss et al. 2002), while under certain conditions, a Kron aperture may only recover half of a galaxy’s total luminosity (Andreon 2002). The Sérsic catalogues are generated from the seeing-uncorrected mosaics, as the seeing parameters are modelled within SIGMA using the PSFEX software utility (E. Bertin, private communication).

### 4.5 Object extraction of Kron and Petrosian apertures

The SExtractor utility (Bertin & Arnouts 1996) is a program that generates catalogues of source positions and aperture fluxes from an input image. It has the capacity to define the sources and apertures in one frame and calculate the corresponding fluxes in a second frame. This dual image mode is computationally more intensive than the standard SExtractor single-image mode (in single-image mode, SExtractor can extract a catalogue from a mosaic within a few hours; dual-image mode takes a few days per mosaic). Using the *u*, *g*, *r*, *i*, *z*, *Y*, *J*, *H* and *K* images created by the SWARP utility, we define our catalogue of sources independently (for the self-defined catalogues), using the *r*-band mosaics (for the *r*-band-defined catalogue) or the *K*-band mosaics (for the *K*-band-defined catalogue), and calculate their flux in all nine bands. The normalization and

SWARP processes removed the image background and standardized the zero-point; we therefore use a constant MAG\_ZEROPOINT = 30 and BACK\_VALUE = 0. SExtractor generates both elliptical Petrosian- ( $2.0R_{\text{Petro}}$ ) and Kron-like apertures ( $2.5R_{\text{Kron}}$ , called AUTO magnitudes). SExtractor Petrosian magnitudes are computed using  $\frac{1}{\nu R_{\text{Petro}}} = 0.2$ , the same parameter as the SDSS. As the mosaics have been transformed on to the AB magnitude system, all magnitudes generated by the GAMA photometric pipeline are AB magnitudes.

The seeing convolution routine smooths out the background and correlates the read noise of the images (this is apparent in Fig. A1). As SExtractor detects objects of  $>x\sigma$  above the background (where  $x$  is a definable parameter set to 1 in the default file and for our seeing unconvolved catalogues), this assists in the detection process, allowing SExtractor to find objects to a much greater depth, thus increasing the number of sources extracted using the standard setup. However, these new objects are generally much fainter than the photometric limits of the GAMA spectroscopic campaign, many are false detections and the time required to generate the source catalogues (particularly using SExtractor in dual-image mode) is prohibitively large. Using a  $10\,000 \times 10\,000$  pixel subset of the GAMA9 *r*-band mosaic, we have attempted to calculate the DETECT\_THRESH parameter that would output a catalogue of approximately the same depth and size as the unconvolved catalogue within our spectroscopic limits (see Section 2.1). The distribution of objects with different DETECT\_THRESH  $\sigma$  parameters, compared to the unconvolved catalogue, is shown in Fig. 6. We use a DETECT\_MINAREA of 9 pixels. As the unconvolved catalogue is slightly deeper than the  $2\sigma$ , but not as deep as the  $1.7\sigma$  convolved catalogue, we use a DETECT\_THRESH parameter of  $1.7\sigma$  to generate our convolved catalogues. The  $1.7$  and  $1\sigma$  catalogues have consistent number counts to  $r_{\text{AUTO}} = 21$  mag, half a magnitude beyond the  $r_{\text{SDSS}}$ -band magnitude limit of the GAMA input catalogue.

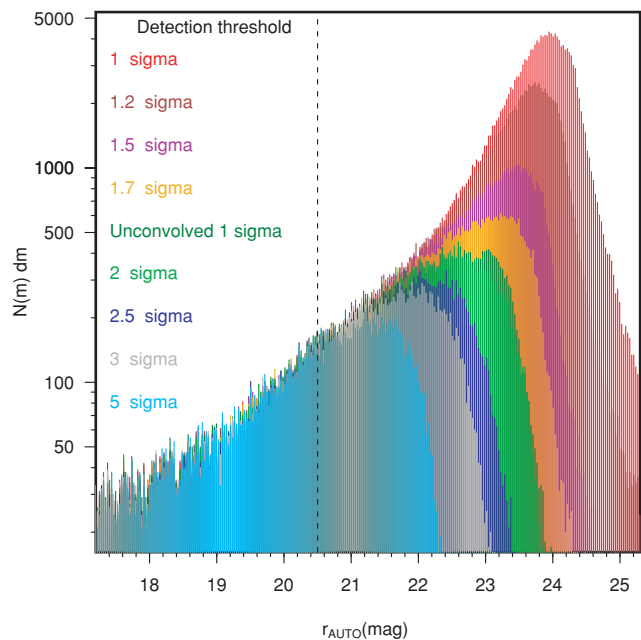


**Figure 6.** The effects of changing the SExtractor DETECT\_THRESH parameter on a subset of an *r*-band mosaic. The dotted black line is the deepest *r*-band sample limit of the GAMA survey (for those objects that are *K* or *z* selected).



**Table 2.** The names of the generated catalogues, the prescription used to create them and their abbreviated filename. The syntax in the Key column is summarized in Section 4.8.

Catalogue name	Key	Abbreviation
<i>r</i> -band-defined catalogue	$r[ugriz]_{\text{SDSS}} + r[ugrizYJHK]_{\text{GAMA:Petro,Kron}}$	catrdef
Self-defined catalogue	$r[ugriz]_{\text{SDSS}} + \{ugrizYJHK\}_{\text{GAMA:Petro,Kron}}$	catsd
<i>K</i> -band-defined catalogue	$r[ugriz]_{\text{SDSS}} + K[ugrizYJHK]_{\text{GAMA:Petro,Kron}}$	catKdef
Sérsic catalogue	$r[ugriz]_{\text{SDSS}} \{ugrizYJHK\}_{\text{GAMA:Sersic}}$	catsers
GAMA master catalogue	$(r[ugriz]_{\text{SDSS}} \{r\}_{\text{GAMA:Sersic}}) + \{ugrizYJHK\}_{\text{GAMA:Petro,Kron}}$	catmast

#### 4.6 Object extraction for Sérsic magnitudes

Sérsic magnitudes are obtained as an output from the galaxy modelling program SIGMA (Structural Investigation of Galaxies via Model Analysis) written in the R programming language (Kelvin et al. 2010). In brief, SIGMA takes the RA and Dec. of an object that has passed our star–galaxy separation criteria and calculates its pixel position within the appropriate mosaic. A square region, centred on the object, is cut out from the mosaic containing a minimum of 20 guide stars with which to generate a PSF. SExtractor then provides a FITS-standard input catalogue to PSF EXTRACTOR (E. Bertin, private communication), which generates an empirical PSF for each image. Ellipticities and position angles are obtained from the STSDAS ELLIPSE routine within IRAF, and provides an input to GALFIT. The larger cutout is again cut down to a region which contains 90 per cent of the target object’s flux plus a buffer of 10 pixels and will only deviate from this size if a bright nearby object causes the fitting region to be expanded in order to model any satellites the target may have.

GALFIT 3 is then used to fit a single-Sérsic component to each target and several runs may be attempted, if, for example, the previous run crashed, the code reached its maximum number of iterations, the centre has migrated to fit a separate object, the effective radius is too high or low or the Sérsic index is too large. SIGMA employs a complex event handler in order to run the code as many times as necessary to fix these problems; however, not all problems can be fixed and so residual quality flags remain to reflect the quality of the final fit. The SIGMA package takes approximately 10 s per object. For full details of the SIGMA modelling program, see Kelvin et al. (2010).

#### 4.7 Catalogue matching

The definition of the GAMA spectroscopic target selection (hereinafter referred to as the tiling catalogue) is detailed in Baldry et al. (2010) and is based on original SDSS DR6 data. We therefore need to relate our revised photometry back to this catalogue in order to connect it to our AAOmega spectra. The tiling catalogue utilizes a mask around bright stars that should remove most objects with bad photometry and erroneously bright magnitudes, as well as implementing a revised star–galaxy separation quantified against our spectroscopic results. It has been extensively tested, with sources that are likely to be artefacts, bad deblends or sections of larger galaxies viewed a number of times by different people. By matching our catalogues to the tiling catalogue, we can access the results of this rigorous filtering process and generate a full, self-consistent set of colours for all of the objects that are within the GAMA sample (and are within regions that have been observed in all nine passbands). As the tiling catalogue is also used when redshift targeting, we will be able to calculate the completeness in all the passbands of the GAMA survey. The GAMA tiling catalogue is a subset of

the GAMA master catalogue (hereinafter referred to as the master catalogue). The master catalogue is created using the SDSS DR6 catalogue stored on the CAS.<sup>2</sup> Unlike the master catalogue, the tiling catalogue undertakes star–galaxy separation and applies surface brightness and magnitude selection.

STILTS (Taylor 2006) is a catalogue combination tool, with a number of different modes. We use it to join our region catalogues together to create *r*-band-defined, *K*-band-defined and self-defined aperture photometry catalogues that cover the entire GAMA area. We also use it to match these catalogues to the GAMA tiling catalogue.

#### 4.8 Source catalogues

The catalogues that have been generated are listed in Table 2. The syntax of the ‘Key’ column is as follows.  $X[u]$  means a *u*-band magnitude from an *X*-band-defined aperture,  $\{u\}$  means a self-defined *u*-band magnitude and ‘+’ denotes a STILTS tskymatch2 5-arcsec, unique nearest-object match between two catalogues (see Section 4.7). Where two data sets are combined together without the ‘+’ notation (i.e. the final two lines), this denotes a STILTS tmatch2, matcher = ‘exact’ match using SDSS objid as the primary key. Note that in a set of self-defined samples ( $\{ugrizYJHK\}$ ), each sample must be matched separately (as each contains a different set of sources) and then combined. This is not the case in the aperture-defined samples (where each sample contains the same set of sources). Subscripts denote the photometric method used for each catalogue.

### 5 TESTING THE GAMA CATALOGUES

In order to test the detection and deblending outcomes within the GAMA catalogues, a subsection of 25 deg<sup>2</sup> has been chosen from near the centre of the GAMA 9 region (the pixels used are 20 000–65 000 in the *x*-direction of the mosaic and 0–45 000 in the *y*-direction). This region was chosen as it contains some of the issues facing the entire GAMA subset, such as area incompleteness. UKIDSS observations miss a large fraction of the subset area – approximately 3.02 deg<sup>2</sup> of the region has incomplete NIR coverage. The subset region was also chosen, because it partially contains an area covered by the *Herschel* ATLAS science verification region (see Eales et al. 2010). Within this region, we ran SExtractor and compared our results with the source lists produced by the SDSS

<sup>2</sup> We use the query `SELECT * FROM dr6.PhotoObj as p WHERE (p.modelmag_r - p.extinction_r < 20.5 or p.petromag_r - p.extinction_r < 19.8) and ((p.ra > 129.0 and p.ra < 141.0 and p.dec > -1.0 and p.dec < 3.0) or (p.ra > 174.0 and p.ra < 186.0 and p.dec > -2.0 and p.dec < 2.0) or (p.ra > 211.5 and p.ra < 223.5 and p.dec > -2.0 and p.dec < 2.0)) and (p.mode = 1) or (p.mode = 2 and p.ra < 139.939 and p.dec < -0.5 and (p.status & dbo.fphotostatus('OK_SCANLINE')) > 0))`.

and UKIDSS extraction software. Unless otherwise specified, all magnitudes in this section were calculated using  $r$ -band-defined apertures.

### 5.1 Numerical breakdown

After generating source catalogues containing self-consistent colours for all objects in the subset region (using the process described in Sections 4.5 and 4.7), we are left with an  $r$ -band aperture-defined subset region catalogue containing 1810 134 sources and a  $K$ -band aperture-defined subset region catalogue containing 2298 224 sources (hereinafter referred to as the  $r$ -band and  $K$ -band catalogues, respectively). These catalogues contain many sources we are not interested in, such as sources with incomplete colour information, sources that are artefacts within the mosaics (satellite trails, diffraction spikes, etc.), sources that are stars and sources that are fainter than our survey limits.

The unfiltered  $r$ - and  $K$ -band catalogues were matched to the master catalogue with a centroid tolerance of 5 arcsec, using the STILTS `tskymatch2` mode (see Section 4.7). Table 3 contains a breakdown of the fraction of matched sources that have credible  $X_{\text{AUTO}}$  and  $X_{\text{PETRO}}$  for all nine passbands (sources with incorrect AUTO or PETRO magnitudes have the value 99 as a placeholder; we impose a cut at  $X = 50$  to remove such objects). Generally, the low quality of the  $u$ -band SDSS images causes problems with calculating extended source magnitudes and this shows itself in the relatively high fraction of incomplete sources. This problem does not affect the other SDSS filters to anywhere near the same extent. SDSS observations do not cover the complete subset area, but they have nearly complete coverage in both the  $r$ -band-defined (which is dependent on SDSS imaging) and the  $K$ -band-defined (reliant on UKIDSS coverage) catalogues. The UKIDSS observations cover a smaller section of the subset region, with the  $Y$  and  $J$  observations (taken separately to the  $H$  and  $K$ ) covering the least area of sky. This is apparent in the  $r$ -band catalogue, where at least 16 per cent of sources lack PETRO or AUTO magnitudes in one or more passbands. By its definition, the  $K$ -band catalogue requires  $K$ -band observations to be present; as such there is a high level of completeness in the  $grizH$  and  $K$  passbands. However, the number of matched SDSS sources in the  $K$ -band catalogue itself is 4.2 per cent lower than in the  $r$ -band catalogue.

**Table 3.** Number of sources within the subset region with good SExtractor  $X_{\text{AUTO}}$  and  $X_{\text{PETRO}}$ , where  $X$  is  $ugrizYJHK$ , from the  $r$ - or  $K$ -band-defined aperture catalogues matched to the GAMA master catalogue. The total number of sources within the GAMA master catalogue for this region of sky is 138 233. per cent Cover is defined relative to  $r$ -band cover; where SDSS coverage does not exist, there are no GAMA master catalogue sources.

Band	per cent Cover	Sources ( $r$ )	per cent ( $r$ )	Sources ( $K$ )	per cent ( $K$ )
Total	–	129 488	–	123 740	–
$u$	100	111 403	86	105 801	86
$g$	100	129 169	100	123 317	100
$r$	100	129 481	100	123 610	100
$i$	100	129 358	100	123 533	100
$z$	100	128 287	99	122 479	99
$Y$	88	108 167	84	109 672	89
$J$	89	109 364	84	109 816	89
$H$	96	121 212	94	121 846	98
$K$	94	118 224	91	122 635	99

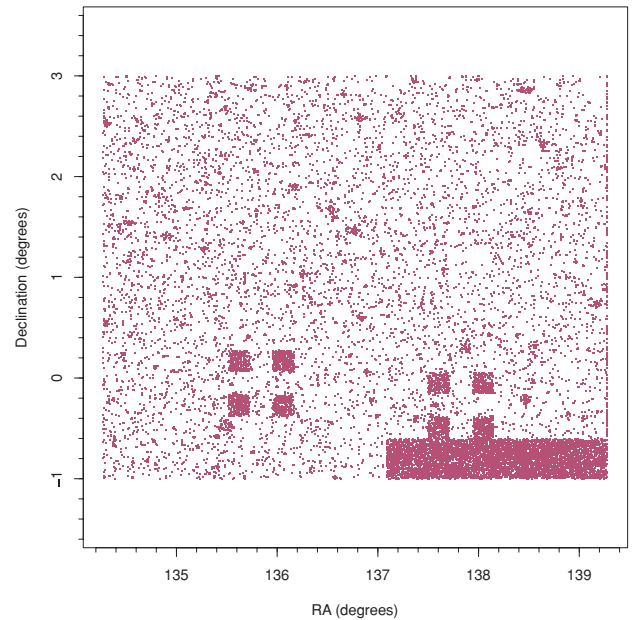


**Figure 7.** The RA and Dec. of SDSS objects that are not in either the  $r$ - or the  $K$ -band master-catalogue-matched catalogue. The darker areas note a high density of unmatched objects.

There are 138 233 master catalogue SDSS sources within the subset region. 119 330 SDSS objects have matches (within a 5-arcsec tolerance) in both the  $r$ - and  $K$ -band master-catalogue-matched catalogues (this number is found by matching SDSS objid between the catalogues). Those SDSS objects that do not have matches in both master-catalogue-matched catalogues are shown in Fig. 7. We detail the reasons for the missing objects in Section 5.2.

### 5.2 SDSS sources missing in the master-catalogue-aperture-matched catalogues

There are 18 903 SDSS sources that are not found when the master catalogue is matched to either the  $r$ -band or the  $K$ -band-defined subset region catalogues, 13.7 per cent of the total number of master catalogue sources within the subset region. Fig. 7 shows their distribution on sky. 8745 sources are not found within the  $r$ -band-defined catalogue (6.3 per cent of the master catalogue sample) and 14 493 are not found within the  $K$ -band-defined catalogue (10.5 per cent of the sample), with 4335 of the sources unmatched to either the  $r$ - or the  $K$ -band-defined sample (3.1 per cent of the master catalogue sample). As the SDSS sample is defined by optical data, it is unsurprising that a far larger number of sources are not found within the  $K$ -band-defined catalogue. Of the 18 903 unmatched master catalogue sources, only 2367 have passed star–galaxy separation criteria and are brighter than the GAMA spectroscopic survey magnitude limits ( $r < 19.8$  or  $zK$  selected).

Using  $r$ -band imaging, we have visually inspected all 8745 SDSS sources where our  $r$ -band-defined subset region catalogue cannot find a match within 5 arcsec. Table 4 contains a summary of the reasons we do not find a  $r$ -band match. Using the SExtractor detection failure rate from the subset region as a guide to the detection failure rate for the entire GAMA region, SExtractor will miss approximately 2.8 per cent of the objects recovered by the SDSS. A second problem was flagged through the inspection process; a further 1.7 per cent of the master catalogue sources within the subset region were not visible. Either these objects are low surface bright-

**Table 4.** A breakdown of the reasons for faulty detections in the 8745 SDSS objects that are not matched to the  $r$ -band subset region catalogue. The images of the SDSS objects were generated from the standard  $r$ -band GAMA mosaics and all 8745 objects were viewed by one observer (DTH). The criteria for selection are as follows. The first category is chosen in those cases where an object has a nearby neighbour or may have been deblended into multiple sources by the SDSS algorithm. The second category is chosen where the position of the object is covered by a spike/trail. The third category is where a source is visible by eye. The fourth category is where a source is not visible above the noise. The fifth category is chosen when a source is obviously part of a larger structure. The sixth category is chosen when the SDSS data are of too low quality for visual classification to be undertaken.

Reason for non-detection	Number of objects	Per cent of GAMA master catalogue subset region sample
Possible deblending mismatch	601	0.4
Saturation spike/satellite or asteroid trail	404	0.3
SEXTRACTOR detection failure	3831	2.8
Either a low surface brightness source or no source	2391	1.7
Part of a large deblended source	1463	1.1
Low image quality making detection difficult	55	0.04

ness extended objects, possibly detected in a different band, or the SDSS object extraction algorithm has made a mistake. A further 1.8 per cent of sources within the GAMA master catalogue will be missed by SEXTRACTOR due to differences in deblending decisions (either failing to split two sources or splitting one large object into a number of smaller parts), low SDSS image quality making SEXTRACTOR fail to detect any objects or an artefact in the image being accounted for by SEXTRACTOR (such as a saturation spike from a large star being detected as a separate object in the SDSS).

### 5.3 Sources in our $r$ -band catalogue that are not in the GAMA master catalogue

To be certain that the SDSS extraction software is giving us a complete sample, we check whether our  $r$ -band subset region catalogue contains sources that should be within the GAMA master catalogue, but are not. There are 61 351 sources within the  $r$ -band-defined subset region catalogue that have a complete set of credible AUTO and PETRO magnitudes, and are brighter than the GAMA spectroscopic survey limits. 619 of these sources do not have SDSS counterparts. We have visually inspected these sources; a breakdown is shown in Table 5. Similar issues cause missing detections using the SDSS or SEXTRACTOR algorithms. However, some of the unseen sources that SEXTRACTOR detected may be due to the image convolution process (Section 3.3) gathering up the flux from a region with high background noise and rearranging it so that it overcomes the detection threshold. Fig. 8 shows the distribution of  $r_{\text{AUTO}} \leq 20.5$  mag sources detected when SEXTRACTOR is run upon an original SDSS image file (covering  $\sim 0.04$  deg<sup>2</sup>) and the sources from the same file after it has undergone the image convolution process. 233 sources are found in the original SDSS frame and three additional sources are included within the convolved frame sample. An examination of two sources that are in the convolved frame data set and not in the original sample shows the effect: these sources have  $r_{\text{AUTO}}$  luminosities of 20.64

**Table 5.** A breakdown of the 619  $r$ -band-defined subset region catalogue objects brighter than the GAMA sample limits that are not matched to the GAMA master catalogue. The images of the subset region catalogue objects were generated from the standard  $r$ -band GAMA mosaics and all 619 objects were viewed by one observer (DTH).

Type of source	Number of objects
Source	171
No visible source	274
Section of bright star	163
Possible deblend mismatch	10
Low image quality making detection difficult	1

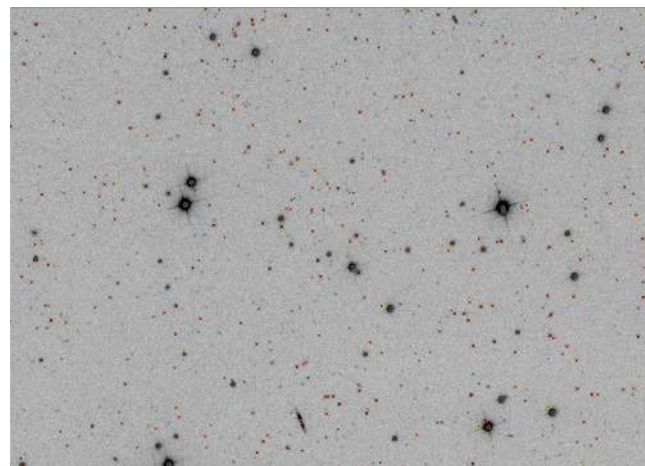


**Figure 8.** A comparison between the objects detected when SEXTRACTOR is run over an original SDSS image and when it is run over the convolved, mosaic imaging. Yellow circles are sources with  $r \leq 20.5$  mag detected from the GAMA mosaic and red crosses are sources that are detected from the original SDSS data.

and 20.77 mag pre-convolution, but  $r_{\text{AUTO}}$  luminosities of 20.40 and 20.48 mag post-convolution.

Taking the SDSS non-detection rate within the subset region to be the same as the non-detection rate over the entire GAMA region, we expect that the SDSS algorithm would have failed to detect 0.1 per cent of sources brighter than the GAMA spectroscopic survey limits; approximately, 1000 sources would not have been included within the master catalogue.

### 5.4 Sources in our $K$ -band catalogue that are not in the UKIDSS DR5PLUS data base

We have also tested the UKIDSS DR5 catalogue. We have generated a catalogue from the WSA that selects all UKIDSS objects within the GAMA subset region<sup>3</sup> and we have matched this catalogue to the  $K$ -band-defined subset region catalogue. From the 69 537  $K$ -band-defined subset region catalogue sources, there are 4548 sources that have not been matched to an UKIDSS object within a tolerance of 5 arcsec. We have visually inspected  $K$ -band images of those objects that are brighter than the GAMA spectroscopic survey  $K$ -band limit ( $K_{\text{AUTO}} \leq 17.6$  mag). We find that 29 of the 117 unmatched objects are real sources that are missed by the UKIDSS extraction

<sup>3</sup> We use the query 'SELECT las.ra, las.dec, las.kPetroMag FROM lasSource as las WHERE las.ra < 139.28 AND las.ra > 134.275 AND las.dec > -1 AND las.dec < 3'.

software, a negligible fraction of the entire data set. A large (but unquantified) fraction of the other 88 sources are suffering from the convolution flux-redistribution problem discussed in Section 5.3. The background fluctuations in  $K$ -band data are greater than in the  $r$  band, making this a much greater problem.

## 6 PROPERTIES OF THE CATALOGUES

### 6.1 Constructing a clean sample

In order to investigate the photometric offsets between different photometric systems, we require a sample of galaxies with a complete set of credible photometry that are unaffected by deblending decisions. This has been created via the following prescription. We match the  $r$ -band-defined aperture catalogue to the GAMA master catalogue with a tolerance of 5 arcsec. We remove any GAMA objects that have not been matched or have been matched to multiple objects within that tolerance (when run in All match mode, STILTS produces a GroupSize column, where a NULL value signifies no group). We then match to the nine self-defined object catalogues, in each case removing all unmatched and multiply matched GAMA objects. As our convolution routine will cause problems with those galaxies that contain saturated pixels, we also remove those galaxies that are flagged as saturated by the SDSS. This sample is then linked to the Sérsic pipeline catalogue (using the SDSS objid as the primary key). We remove all those Sérsic magnitudes where the pipeline has flagged that the model is badly fitted or where the photometry has been compromised and match the  $K$ -band aperture-defined catalogue, again with unmatched and multiple matched sources removed. This gives us a final population of 18 065 galaxies that have clean  $r$ -band-defined,  $K$ -band-defined, self-defined and Sérsic magnitudes, are not saturated and cannot be mismatched. Having constructed a clean, unambiguous sample of common objects, any photometric offset can only be due to differences between the photometric systems used. As we remove objects that are badly fitted by the Sérsic pipeline, it should be noted that the resulting sample will, by its definition, only contain sources that have a light profile that can be fitted using the Sérsic function.

### 6.2 Photometric offset between systems

Figs 9–14 show the dispersion between different photometric systems produced by this sample. In Fig. 9, we compare Kron and Petrosian magnitudes; in all other figures, we compare the photometric system to SDSS PETROMAG. In all photometry systems, the  $gri$  relationships are tightest, with the  $u$  and  $z$  relationships subject to a greater scatter, breaking down almost entirely for Figs 12 and 13. The correlation between the SDSS PETROMAG and the  $r$ -band-defined Petrosian magnitude (Fig. 11) looks much tighter than that between the SDSS PETROMAG and the self-defined Petrosian magnitude (Fig. 12). The standard deviations of the samples are similar, with marginally more scatter in the self-defined sample (0.129 mag against 0.148 mag). The median offset between SDSS Petrosian and the  $r$ -band-defined Petrosian magnitudes, however, is 0.01 mag greater.

Fig. 13, illustrating the relationship between the Sérsic magnitude and the SDSS PETROMAG, produces median  $\Delta m_{\text{SDSS}} - m_{\text{Sérsic}}$  values of 0.12, 0.06, 0.06, 0.07 and 0.09 mag in  $ugriz$ . These values can be compared to those presented in fig. 13 of Blanton et al. (2003) (−0.14, 0.00, 0.06, 0.09 and 0.14 mag at  $z = 0.1$ , using the  $^{0.1}ugriz$  filters), given the variance in the relationship (the standard deviations in our samples are 0.77, 0.28, 0.21, 0.22 and 0.40 mag,

respectively). A significant fraction ( $\sim 28$  per cent) of the sample has  $r_{\text{SDSS}} - r_{\text{Sérsic}} > 0.5$  mag and therefore lies beyond the boundaries of this image. These offsets are significant and will be discussed further in Section 7. We can say that the  $r$ -band-defined aperture photometry is the closest match to SDSS PETROMAG photometry. Fig. 14 shows the relationship between the GAMA Sérsic magnitude and the optimal model magnitude provided by the SDSS (CMODEL). The model magnitudes match closely, with negligible systematic offset between the photometric systems in  $gri$ .

### 6.3 Colour distributions

In order to identify the optimal photometric system, we assume that intrinsic colour distribution of a population of galaxies can be approximated by a double-Gaussian distribution (the superposition of a pair of Gaussian distributions with different mean and standard deviation parameters). This distribution can model the bimodality of the galaxy population. The presence of noise will broaden the distribution; hence, the narrowest colour distribution reveals the optimal photometric system for calculating the colours of galaxies and therefore deriving accurate SEDs. Fig. 15 shows the ( $u - r$ ) and ( $r - K$ ) colour distributions for each photometric system, for objects within our subset region. In order to calculate the dispersion in the colour distribution, we generate colour-distribution histograms (with bins of 0.1 mag) and find the double-Gaussian distribution parameters that best fit each photometric system. The best-fitting standard deviation parameters for each sample are shown at the bottom of each plot and are denoted by  $\sigma_{X,1}$  and  $\sigma_{X,2}$  (where  $X$  is the photometric system fitted). The sample with the smallest set of  $\sigma$  parameters should provide the optimal photometric system.

The SDSS, GAMA  $r$ -band-defined aperture and GAMA  $K$ -band-defined distributions (the first, third and fourth diagrams on the top two rows) show a very similar pattern, a tight distribution of objects with a small number of red outliers. As expected, when we use apertures that are defined separately in each filter (the second diagram on the top two rows), the colour distribution of the population is more scattered ( $\sigma_{\text{Petro},1} = 0.7576$  mag,  $\sigma_{\text{Petro},2} = 0.7919$  mag,  $\sigma_{\text{AUTO},1} = 0.5886$  mag,  $\sigma_{\text{AUTO},2} = 0.7086$  mag) and does not show the bimodality visible in the matched aperture photometry (at the bright end of the distribution, there are two distinct subpopulations – one subpopulation above  $u - r = 2$  mag and the other below). For the same reason, and probably because of the low quality of the observations, the ( $u - r$ ) plot using the Sérsic magnitudes (the final diagram on the top row) has the broadest colour distribution ( $\sigma_{\text{Sérsic},1} = 0.6242$  mag,  $\sigma_{\text{Sérsic},2} = 1.098$  mag), although it is well behaved in ( $r - K$ ).

To generate a series of ( $r - K$ ) colours using the UKIDSS survey (leftmost plot on the bottom two rows), we have taken all galaxies within the UKIDSS catalogue<sup>4</sup> and match them (with a maximum tolerance of 5 arcsec) to a copy of the tiling catalogue that had previously been matched with the  $K$ -band aperture-defined catalogue. The distribution of ( $r - K$ ) colours taken from the SDSS and UKIDSS survey catalogues is the first diagram on the bottom two rows of the image. As the apertures used to define the UKIDSS and SDSS sources are not consistent, we find that the tightest ( $r - K$ ) distribution comes from the GAMA  $K$ -band-defined

<sup>4</sup> We run a query at the WSA on UKIDSSDR5PLUS looking for all objects within our subset region with  $\text{lasSource.pGalaxy} > 0.9$  and  $\text{lasSource.kPetroMag} < 20$  – equivalent to  $K_{\text{AB}} < 21.9$  mag.

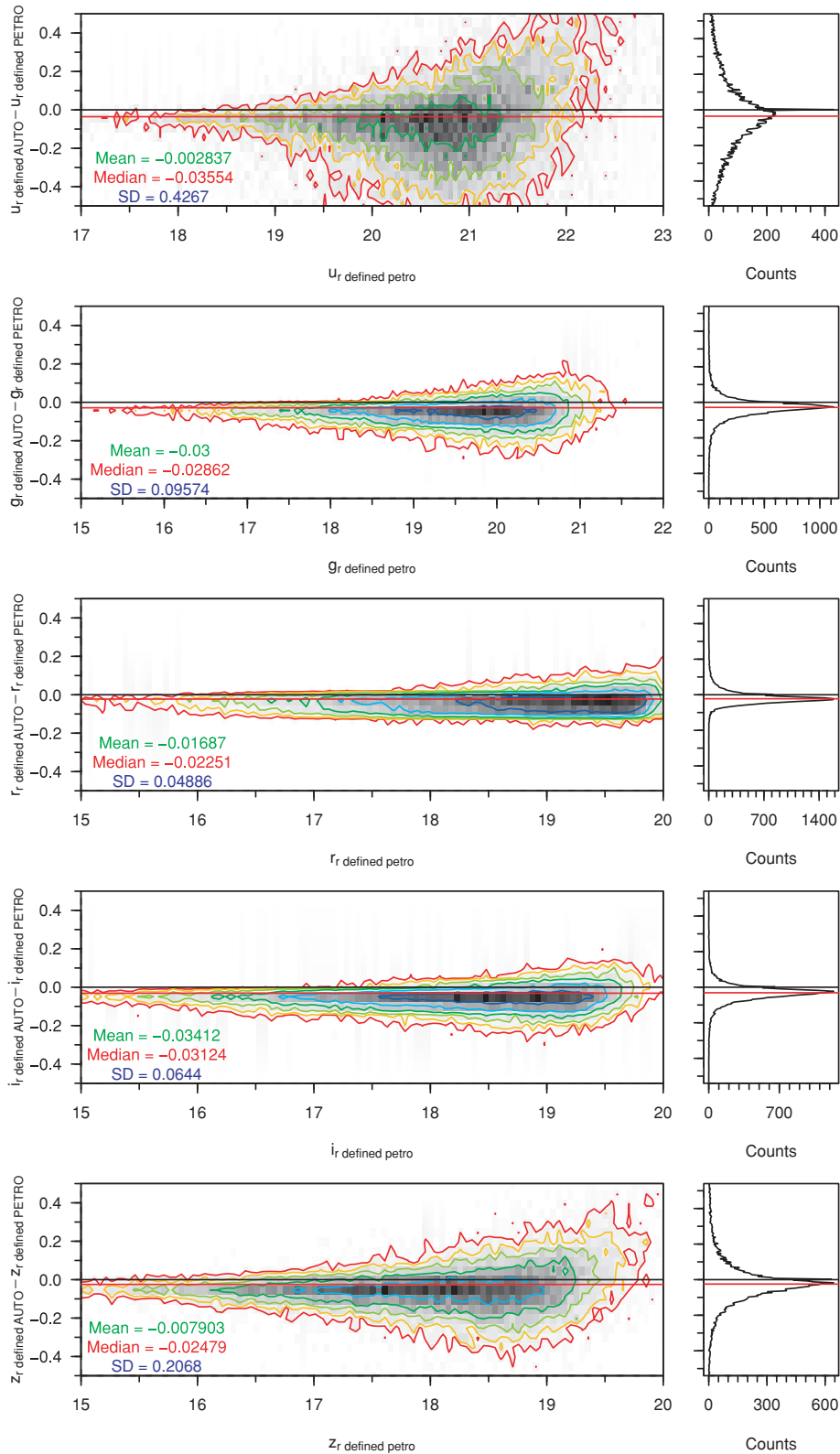


**Figure 9.** GAMA  $r$ -band-defined aperture Petrosian minus AUTO magnitudes for a clean sample of galaxies in  $ugriz$ . Contours are for 4–512 galaxies per bin, rising geometrically in powers of 2. Bins are  $0.05 \text{ mag} \times 0.05 \text{ mag}$  in size.

aperture sample (fourth from the left-hand side on the bottom row, with  $\sigma_{\text{AUTO},1} = 0.3137 \text{ mag}$ ,  $\sigma_{\text{AUTO},2} = 0.4921 \text{ mag}$ ). The GAMA sample that relies on matching objects between self-defined object catalogues (the second diagram on the bottom two rows) has the

broadest distribution ( $\sigma_{\text{Petro},1} = 0.3359 \text{ mag}$ ,  $\sigma_{\text{Petro},2} = 0.6015 \text{ mag}$ ). The distribution of sources in the Sérsic ( $r - K$ ) colour plot is much tighter than in  $(u - r)$ , though still not as tight as the distribution in the fixed aperture photometric systems ( $\sigma_{\text{Sersic},1} = 0.364 \text{ mag}$ ,

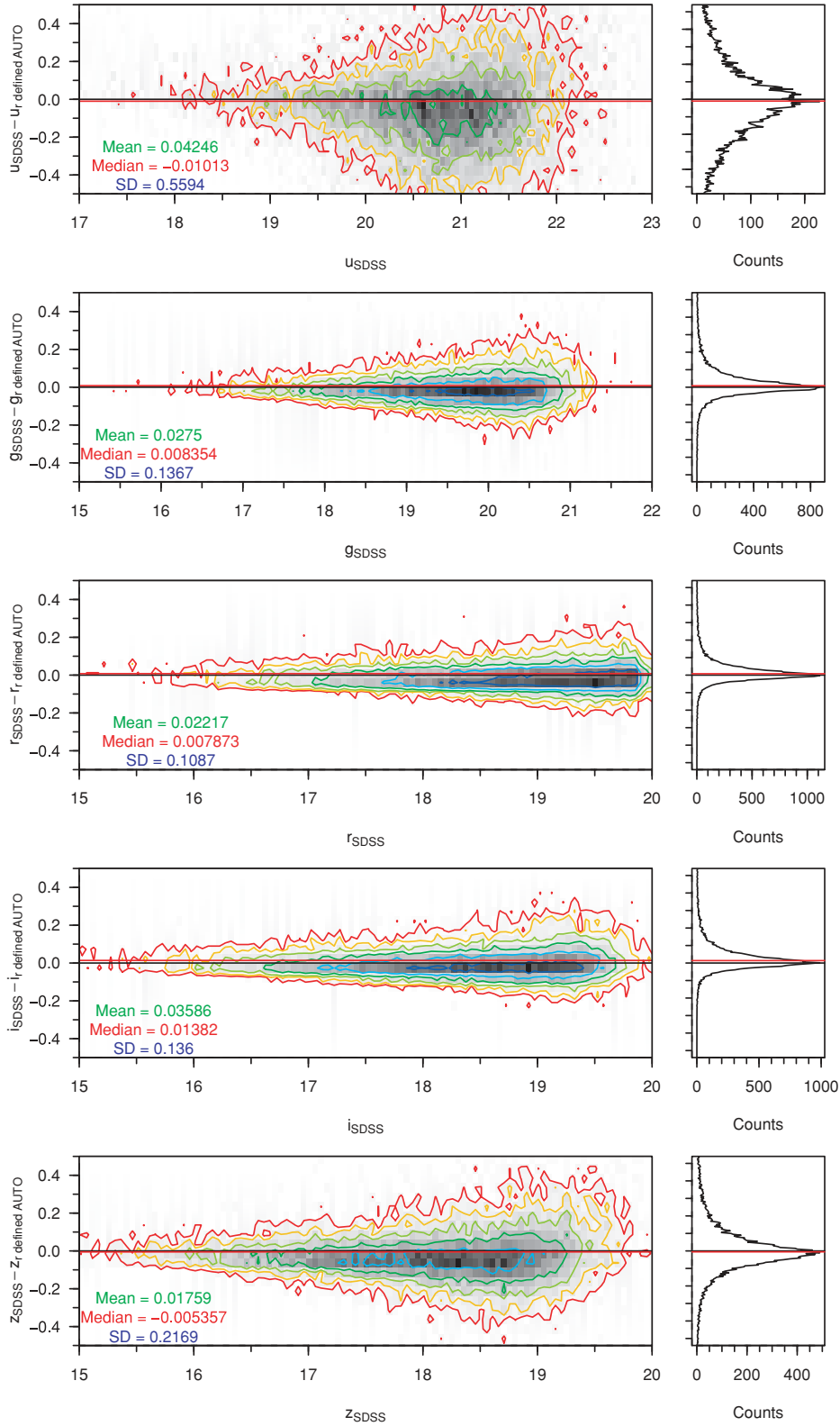


**Figure 10.** SDSS PETROMAG minus GAMA  $r$ -band-defined aperture AUTO magnitudes for a clean sample of galaxies in  $ugriz$ . Contours are for 4–512 galaxies per bin, rising geometrically in powers of 2. Bins are  $0.05 \text{ mag} \times 0.05 \text{ mag}$  in size.

$\sigma_{\text{Sersic},2} = 0.6159 \text{ mag}$ ). Fig. 15 confirms the utility of the GAMA method: by redoing the object extraction ourselves, we have generated self-consistent colour distributions based on data taken by multiple instruments that have a far smaller scatter than a match be-

tween the survey source catalogues ( $\sigma_{\text{SDSS}+\text{UKIDSS},1} = 0.3342 \text{ mag}$ ,  $\sigma_{\text{SDSS}+\text{UKIDSS},2} = 0.5807 \text{ mag}$ ).

We provide one more comparison between our colour distribution and that provided by SDSS and UKIDSS survey data. Fig. 16

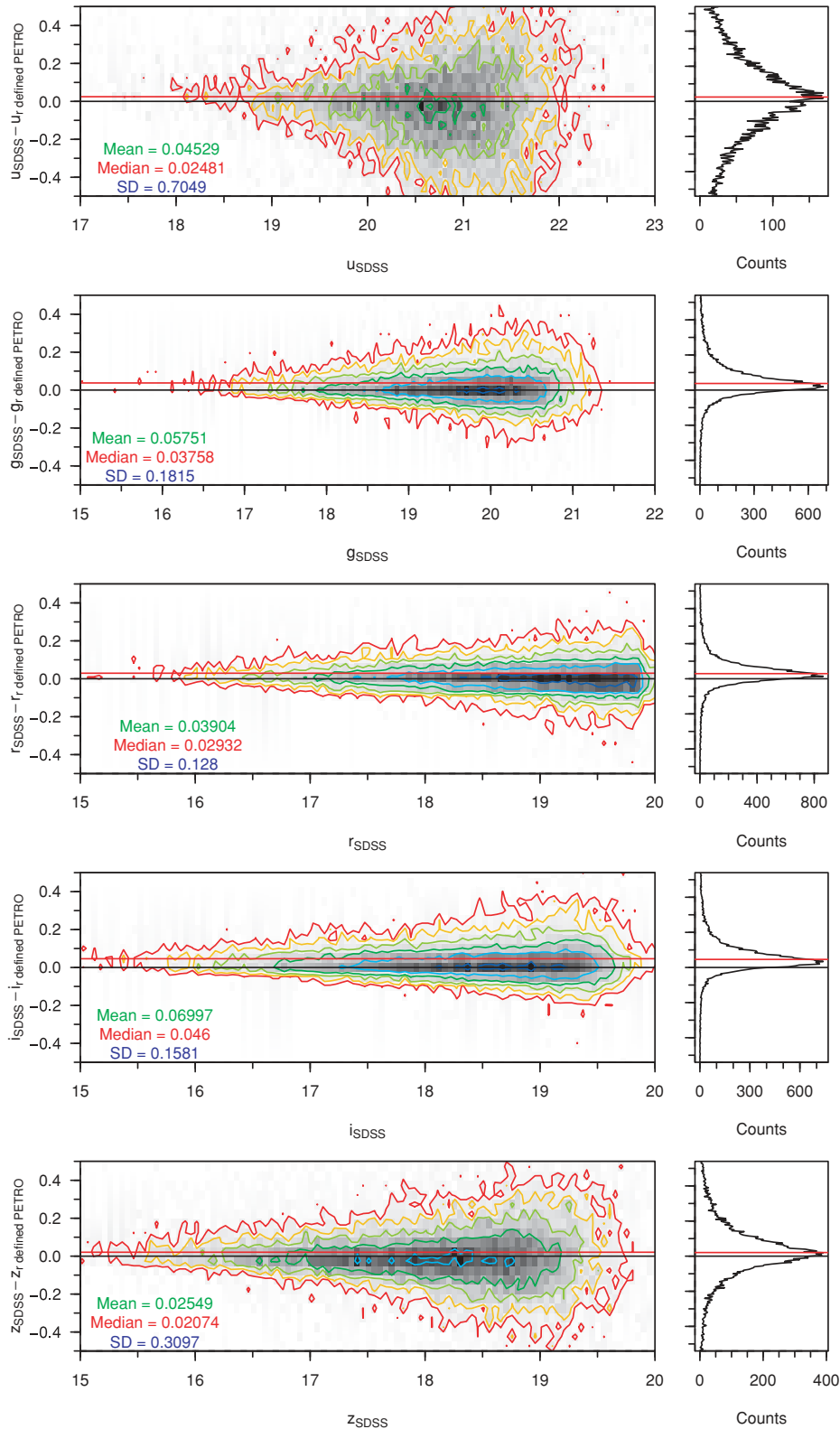


**Figure 11.** SDSS PETROMAG minus GAMA  $r$ -band-defined aperture Petrosian magnitudes for a clean sample of galaxies in  $ugriz$ . Contours are for 4–512 galaxies per bin, rising geometrically in powers of 2. Bins are  $0.05 \text{ mag} \times 0.05 \text{ mag}$  in size.

displays the  $X - H$  distribution produced by the GAMA galaxies with complete  $ugrizYJHK$  photometry and good-quality redshifts within  $0.033 < z < 0.6$ . The effective wavelengths of the filter set for each galaxy are shifted using the redshift of the

galaxy. The colour distribution provided by the GAMA photometry produces fewer outliers than the SDSS/UKIDSS survey data sample and is well constrained by the Bruzual & Charlot (2003) models.

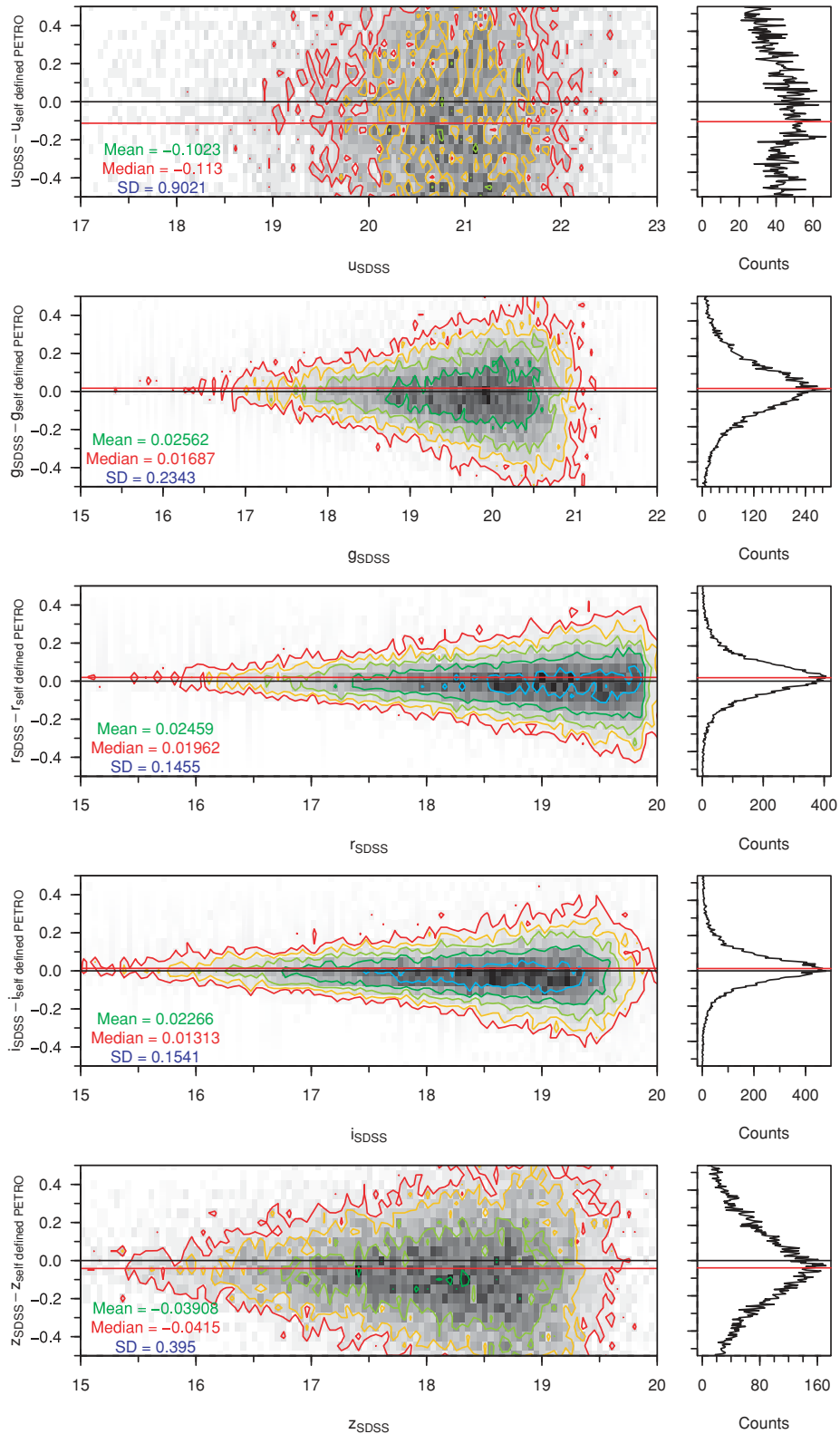


**Figure 12.** SDSS PETROMAG minus GAMA self-defined aperture Petrosian magnitudes for a clean sample of galaxies in *ugriz*. Contours are for 4–512 galaxies per bin, rising geometrically in powers of 2. Bins are  $0.05 \text{ mag} \times 0.05 \text{ mag}$  in size.

## 7 FINAL GAMA PHOTOMETRY

Sections 5 and 6 show that the optimal deblending outcome is produced by the original SDSS data, but the best colours come

from our *r*-band-defined aperture photometry (Section 6.3). We see that our *r*-band-defined aperture photometry agrees with the SDSS PETROMAG photometry. However, we have also demonstrated that SDSS PETROMAG misses flux when compared to our Sérsic total



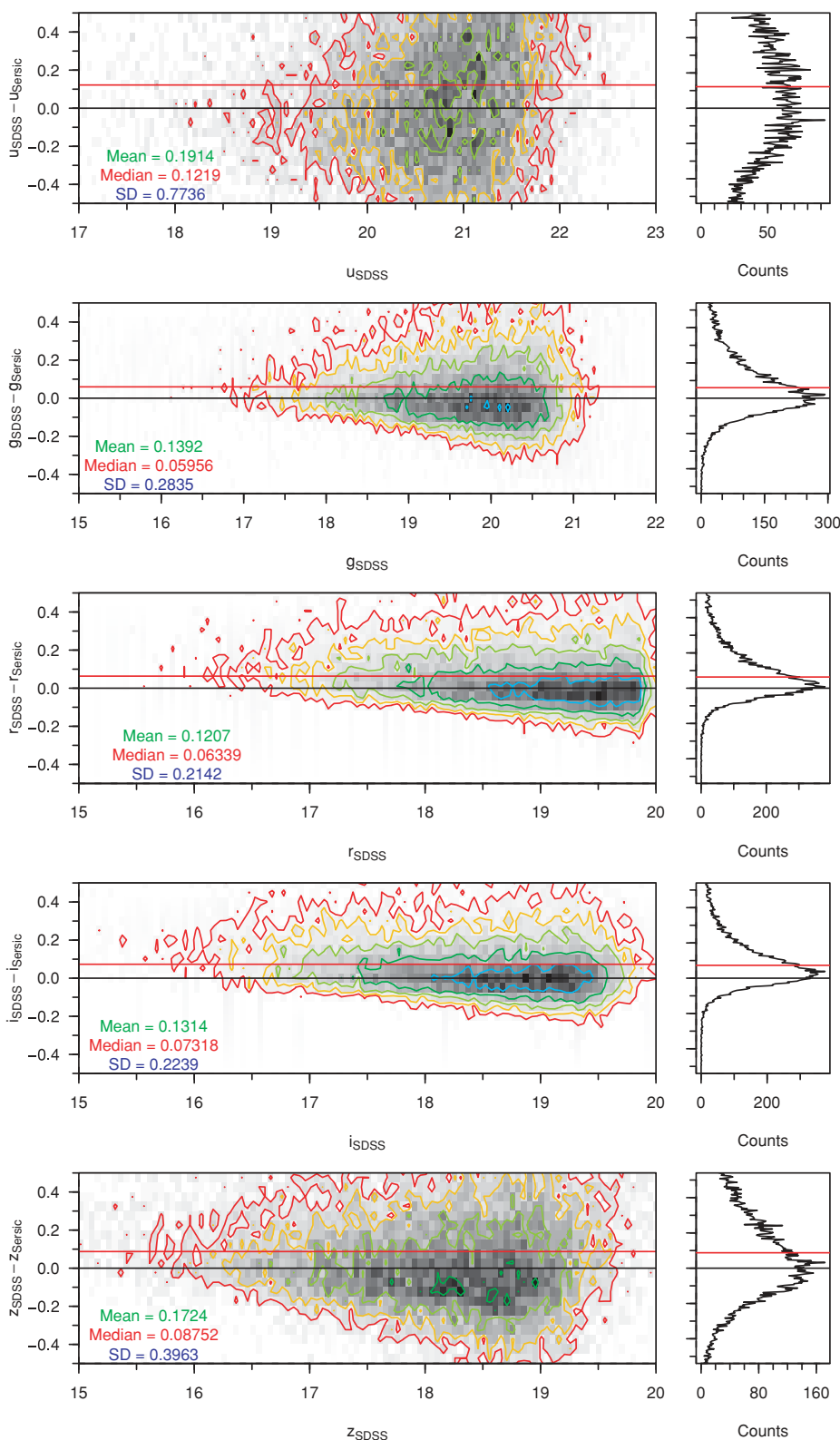


**Figure 13.** SDSS PETROMAG minus GAMA Sérsic magnitudes for a clean sample of galaxies in *ugriz*. Contours are for 4–512 galaxies per bin, rising geometrically in powers of 2. Bins are 0.05 mag  $\times$  0.05 mag in size.

magnitude. Here we combine these data sets to arrive at our final photometry. We combine the SDSS deblending outcome with our *r*-band-defined aperture colours and the Sérsic total magnitude to produce our best photometric solution.

### 7.1 Sérsic magnitudes

To check the reliability of the Sérsic photometry pipeline, we must examine its distribution against a photometric system we

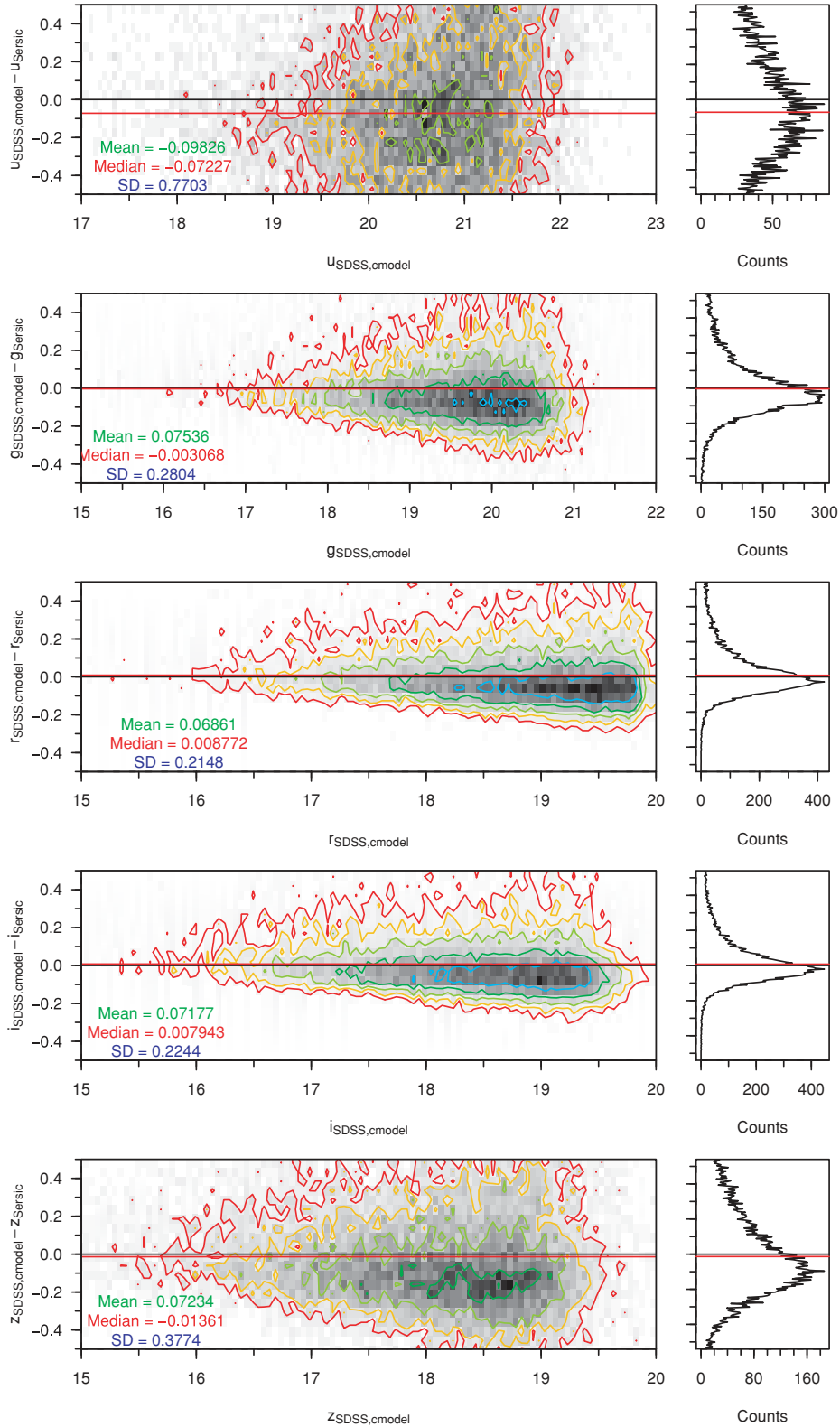


**Figure 14.** SDSS *cmodel* minus GAMA Sérsic magnitudes for a clean sample of galaxies in *ugriz*. Contours are for 4–512 galaxies per bin, rising geometrically in powers of 2. Bins are  $0.05 \text{ mag} \times 0.05 \text{ mag}$  in size.

consider reliable. We examine the distribution of the Sérsic photometry against our *r*-band-defined AUTO photometry. Fig. 17 shows the distribution of Sérsic–GAMA *r*-band-defined AUTO magnitude against *r*-band-defined AUTO magnitude for all objects in the

GAMA sample that have passed our star–galaxy separation criteria and have credible AUTO magnitudes. Whilst there is generally a tight distribution, the scatter in the *u* band, in particular, is a cause for concern.

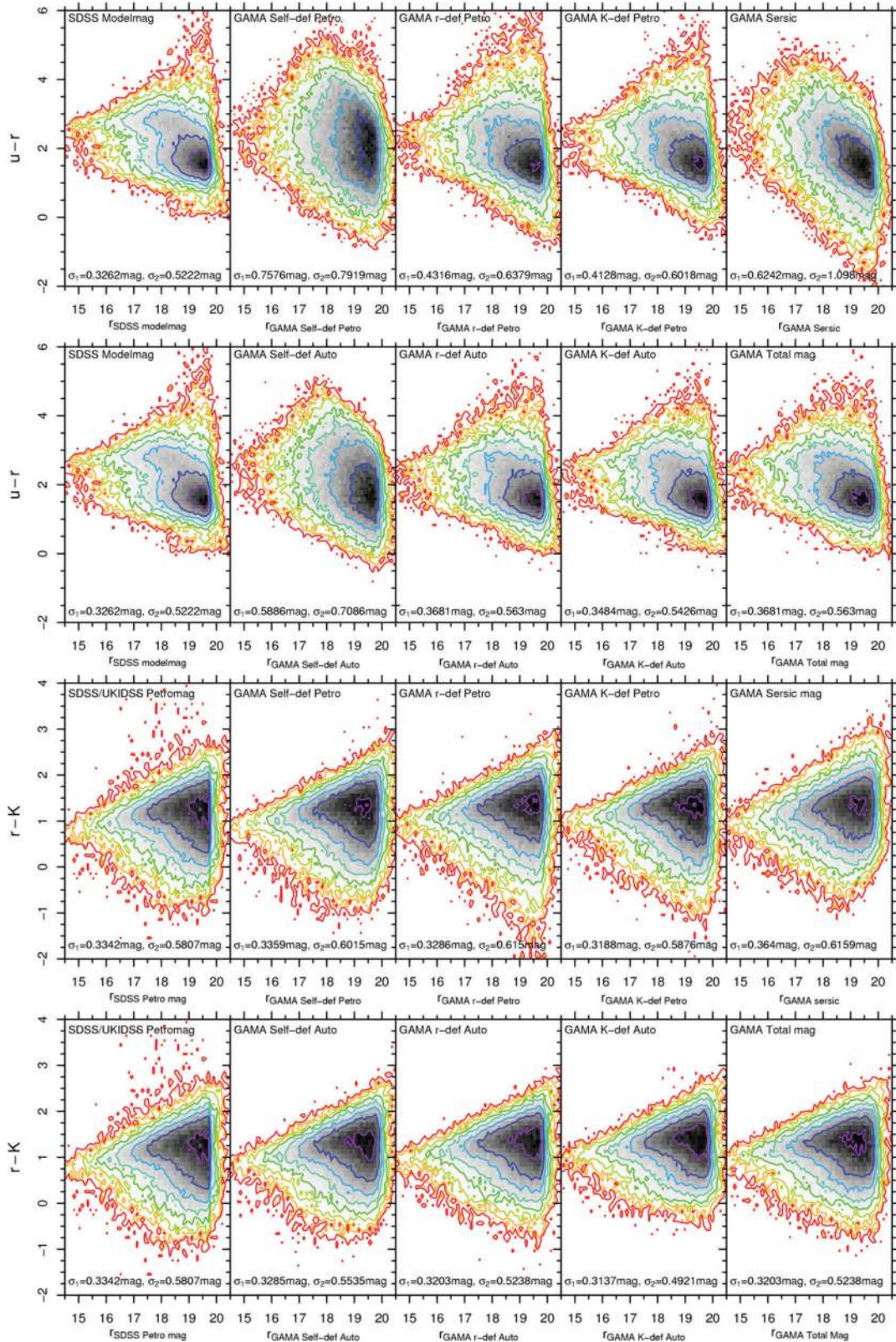


**Figure 15.** A comparison between the  $u-r$  and  $r-K$  colours produced using SDSS MODELmag, GAMA self-defined Petrosian magnitudes, GAMA  $r/K$ -band-defined Petrosian magnitudes, Sérsic and GAMA total magnitudes for objects in the subset region. Contours shown are for 2–512 galaxies per bin, rising geometrically in powers of 2. Bins are 0.1 mag in width in each axis. The  $\sigma$  parameter comes from the best-fitting bivariate-Gaussian distribution, when it is fitted to the colour-distribution histogram in each plot.

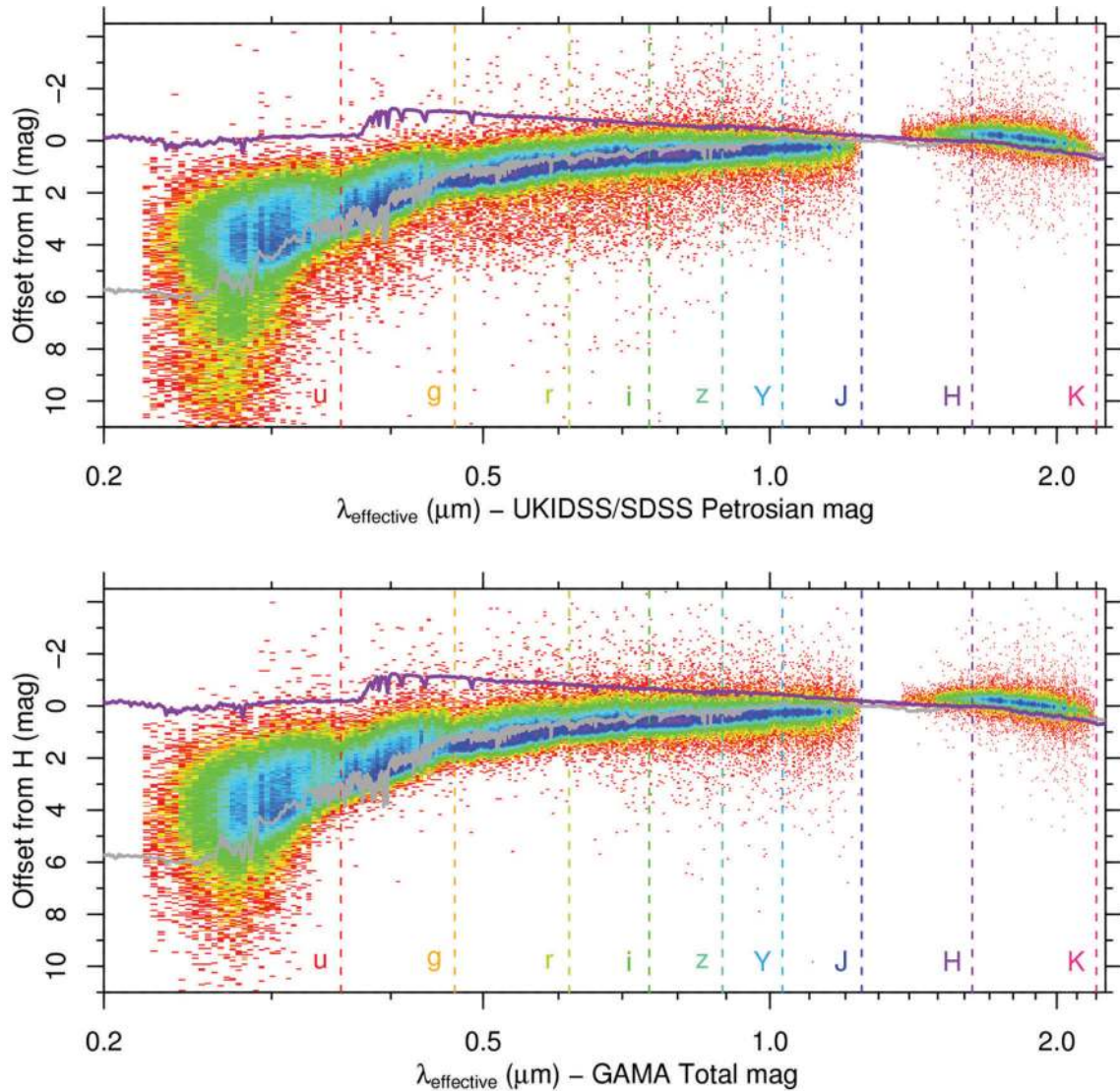


**Figure 16.** A comparison between the  $X - H$  colours produced using SDSS magnitudes and GAMA total magnitudes. Data come from all GAMA galaxies with good-quality redshifts ( $0.033 < z < 0.6$ ) and complete  $ugrizYJK$  photometry. Effective wavelengths are calculated from the redshift of the galaxy and the filter effective wavelength, and the data set is binned into a  $50 \times 50$  bin matrix. Two Bruzual-Charlot 03 SSP instantaneous-burst models are also plotted. Both models use the Chabrier (2003) initial mass function, with mass cut-offs at  $0.1$  and  $100 M_{\odot}$ . Stellar evolution is undertaken using the Padova 1994 prescription. The dark grey line is a model evolved to  $11$  Gyr, with  $Z = 0.05$  and  $Y = 0.352$ . The purple line is a model evolved to  $0.25$  Gyr, using  $Z = 0.02$  ( $Z_{\odot}$ ) and  $Y = 0.28$ .

Graham et al. (2005) analytically calculate how the ratio of Sérsic flux to Petrosian flux changes with the Sérsic index of the object. The fraction of light missed by a Petrosian aperture is dependent upon the light profile of the source. Fig. 19 shows the distribution of Sérsic–GAMA  $r$ -band-defined Petrosian magnitude against the Sérsic index, redshift, absolute and apparent magnitude for all  $r$ -band objects in the GAMA sample that have passed our star-galaxy separation criteria, and have credible  $r$ ,  $u$  and  $K$   $r$ -band-defined PETRO magnitudes. Graham et al. report a  $0.20$ -mag offset for an  $n = 4$  profile and a  $0.50$ -mag offset for an  $n = 8$  profile. The median  $r_{\text{Sérsic}} - r_{\text{Petrosian}}$  offset for objects with  $3.9 < n < 4.1$  in this sample is  $-0.115$  mag, with rms scatter of  $0.212$  mag, and  $-0.408$  mag, for objects with  $7.9 < n < 8.1$ , with rms scatter of  $0.292$  mag. Both results agree with the reported values. We have plotted the magnitude offset with Sérsic index function from fig. 2 (Panel a) of Graham et al. (2005) in the uppermost plot of Fig. 19.

The function is an extremely good match to our photometry. Fig. 18 shows the distribution of Sérsic–SDSS  $r$ -band-defined Petrosian magnitude against the Sérsic index, redshift, absolute and apparent magnitude for all  $r$ -band objects in the GAMA sample that have passed our star-galaxy separation criteria, and have credible  $r$ ,  $u$  and  $K$   $r$ -band-defined PETRO magnitudes. The distributions are very similar to those produced by the Sérsic–Petrosian colours in Fig. 19. An exception is the distribution with the Sérsic index, where the Sérsic–GAMA offset is distributed closer to  $0$  mag, until  $n = 4$ , at which point the Sérsic magnitude detects more flux. As the  $r$ -band magnitude is defined as a combination of  $n = 1$  and  $n = 4$  profiles, it is unsurprising that it cannot model high- $n$  profile sources as well as the GAMA Sérsic magnitude, which allows the  $n$ -parameter greater freedom.

The  $r$ -band Sérsic magnitude shows no anomalous behaviour. Sérsic profiling is reliable when undertaken using the higher

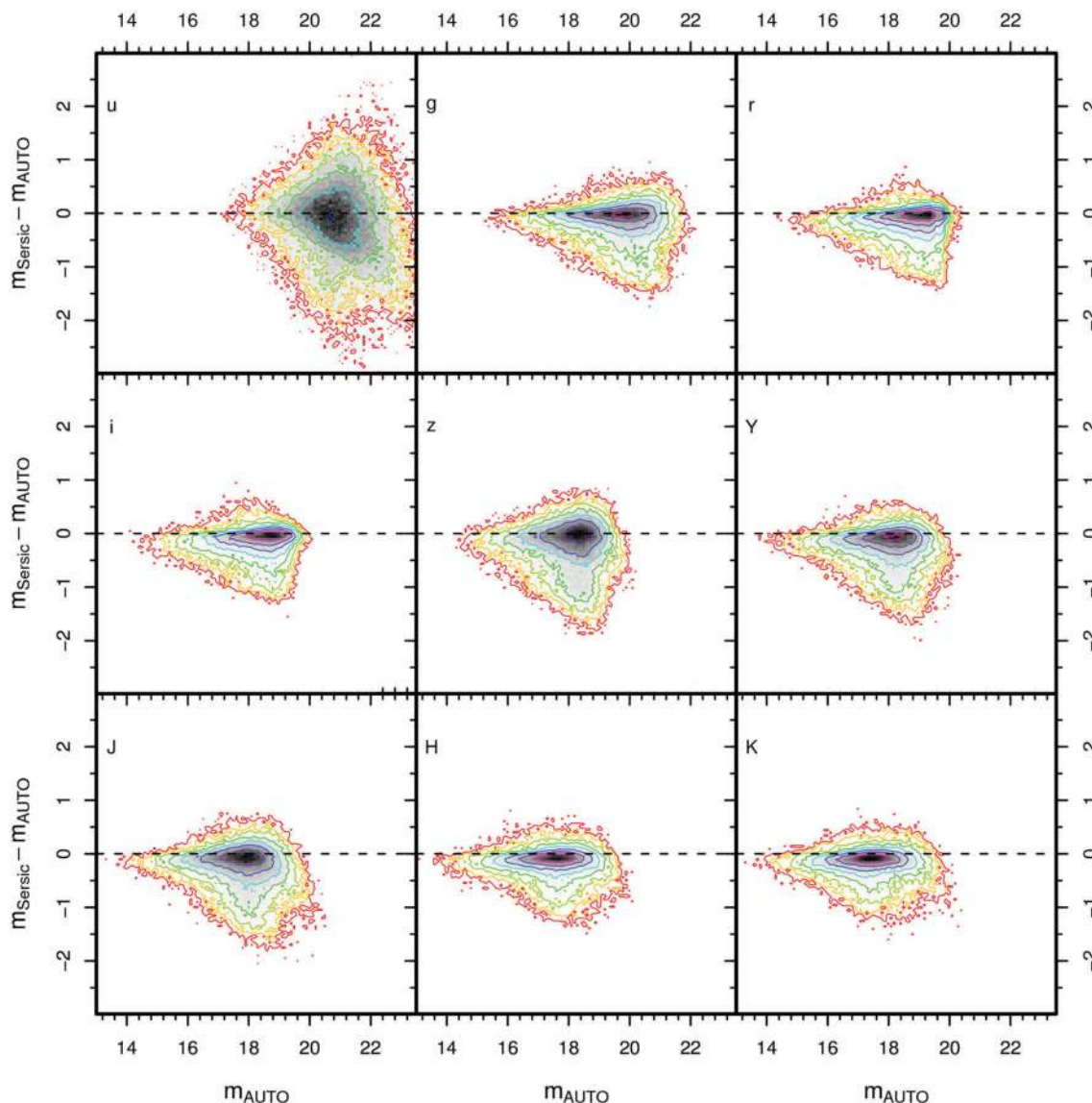


**Figure 17.** Sérsic minus GAMA  $r$ -band-defined AUTO magnitude against  $r$ -band-defined AUTO magnitude, in all nine bands, for all objects in the GAMA sample that pass our star–galaxy separation criteria and have credible  $ugrizYJHK$   $r$ -band-defined AUTO magnitudes. Contours increase geometrically in powers of 2, from 4 to 512. Bins are  $0.1 \text{ mag (x-axis)} \times 0.05 \text{ mag (y-axis)}$  in size.

quality SDSS imaging (particularly  $gri$ ), but not when using the noisier  $u$ -band data. It is clear that the  $u$ -band Sérsic magnitude is not robust enough to support detailed scientific investigations. In order to access a Sérsic-style total magnitude in the  $u$  band, we are therefore forced to create one from existing, reliable data. We devise such an approach in Section 7.2.

## 7.2 ‘Fixed aperture’ Sérsic magnitudes

As mentioned in Section 4.4, the Sérsic magnitude is taken from a different aperture in each band. We therefore cannot use Sérsic magnitudes to generate accurate colours (the scatter in the Sérsic colours is compared to that in the AUTO colours in Fig. 20). We also do not consider the  $u$ ,  $b$  and Sérsic magnitudes to be credible (see Section 7.1). However, we also believe that the  $r$ -band Sérsic luminosity function may be more desirable than the light-distribution-defined aperture  $r$ -band luminosity functions. The calculation of the total luminosity density using a non-Sérsic aperture system may under-

estimate the parameter. We require a system that accounts for the additional light found by the Sérsic magnitude, but also provides a credible set of colours.

We derive a further magnitude  $X_{\text{total}}$ , using the equation  $X_{\text{total}} = (X_{\text{AUTO}} - r_{\text{AUTO}}) + r_{\text{Sérsic}}$ , where ‘AUTO’ is the  $r$ -band-defined AUTO magnitude. In effect, this creates a measure that combines the total  $r$ -band flux with optimal colours, using SDSS deblending to give us the most accurate catalogue of sources (by matching to the GAMA master catalogue); the best of all possibilities. We accept that this assumes that the colour from the  $r$ -band-defined AUTO aperture would be the same as the colour from a  $r$ -band-defined Sérsic aperture; however, this is the closest estimation to a fixed Sérsic aperture we can make at this time.

## 7.3 Uncertainties within the photometry

The gain value in SDSS data is constant within each stripe, but varies between stripes. The SDSS mosaic creation process that is

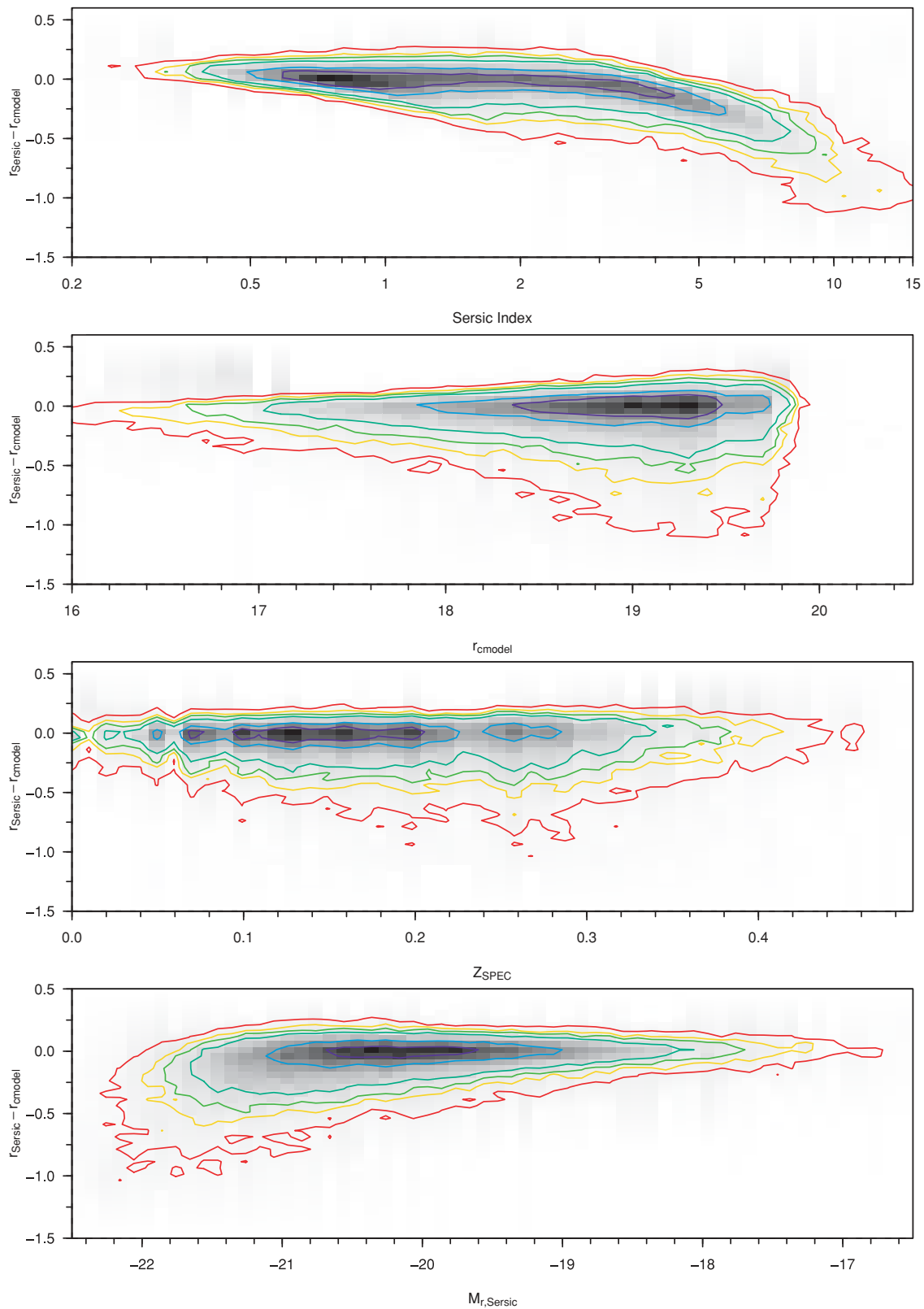


**Figure 18.** Sérsic  $r -$  SDSS cMODEL  $r$  magnitude against the Sérsic index, SDSS  $r$  cMODEL magnitude,  $z$ ,  $M_{r,\text{Sérsic}}$  for all objects in the GAMA sample that have passed our star–galaxy separation criteria and have credible  $urK$   $r$ -band-defined Petrosian magnitudes. Contours increase geometrically in powers of 2, from 4 to 512.

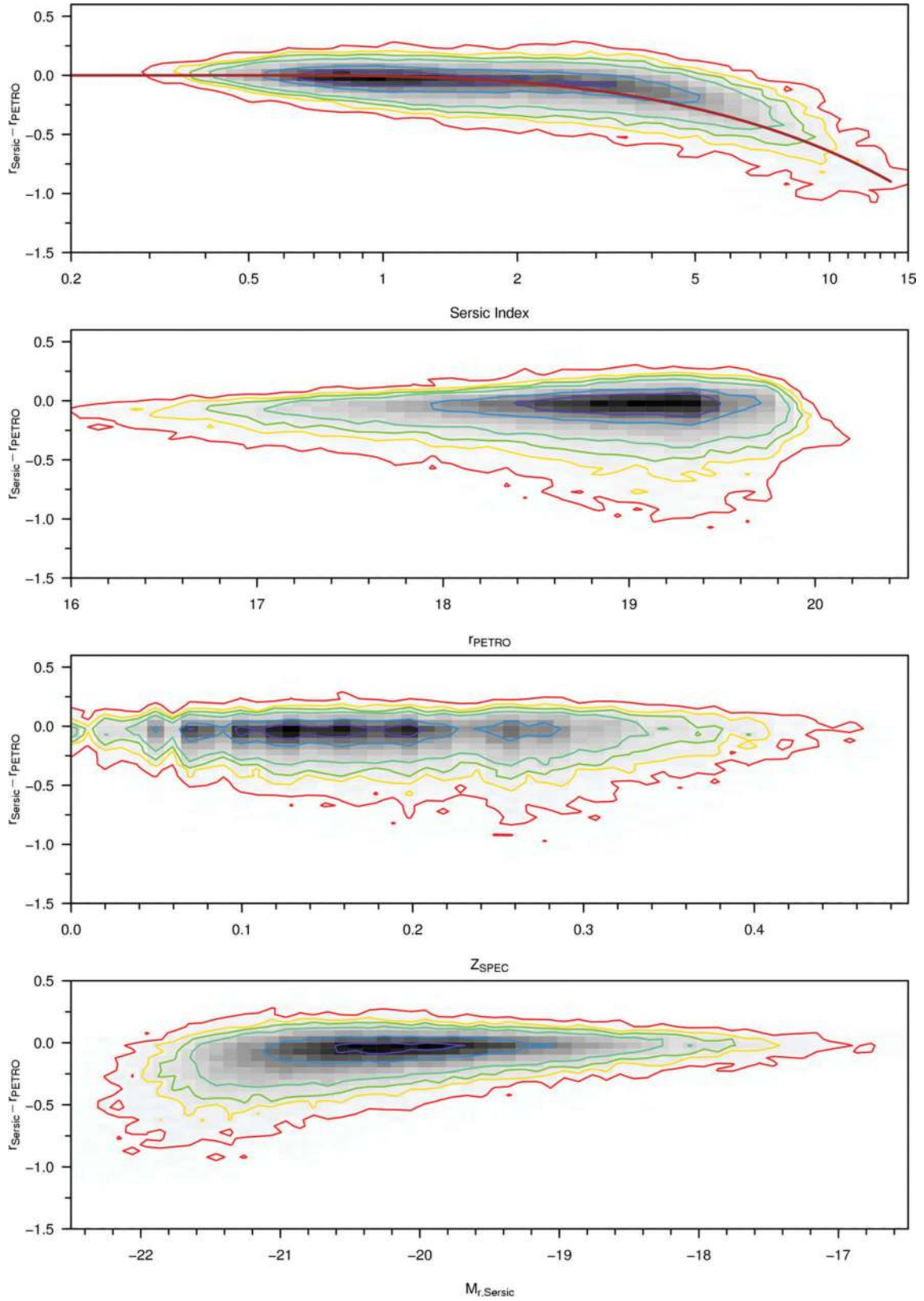


**Figure 19.** Sérsic  $r$  – GAMA  $r$ -band-defined Petrosian  $r$  against the Sérsic index,  $r$ -band-defined  $r$ -band Petrosian magnitude,  $z$ ,  $M_{r,Sérsic}$  for all objects in the GAMA sample that have passed our star–galaxy separation criteria and have credible  $urK$   $r$ -defined Petrosian magnitudes. Contours increase geometrically in powers of 2, from 4 to 512. The brown function plotted in the Sérsic  $r$  – GAMA  $r$ -band-defined Petrosian  $r$  against the Sérsic index plot is taken from fig. 2 (upper panel) of Graham et al. (2005).

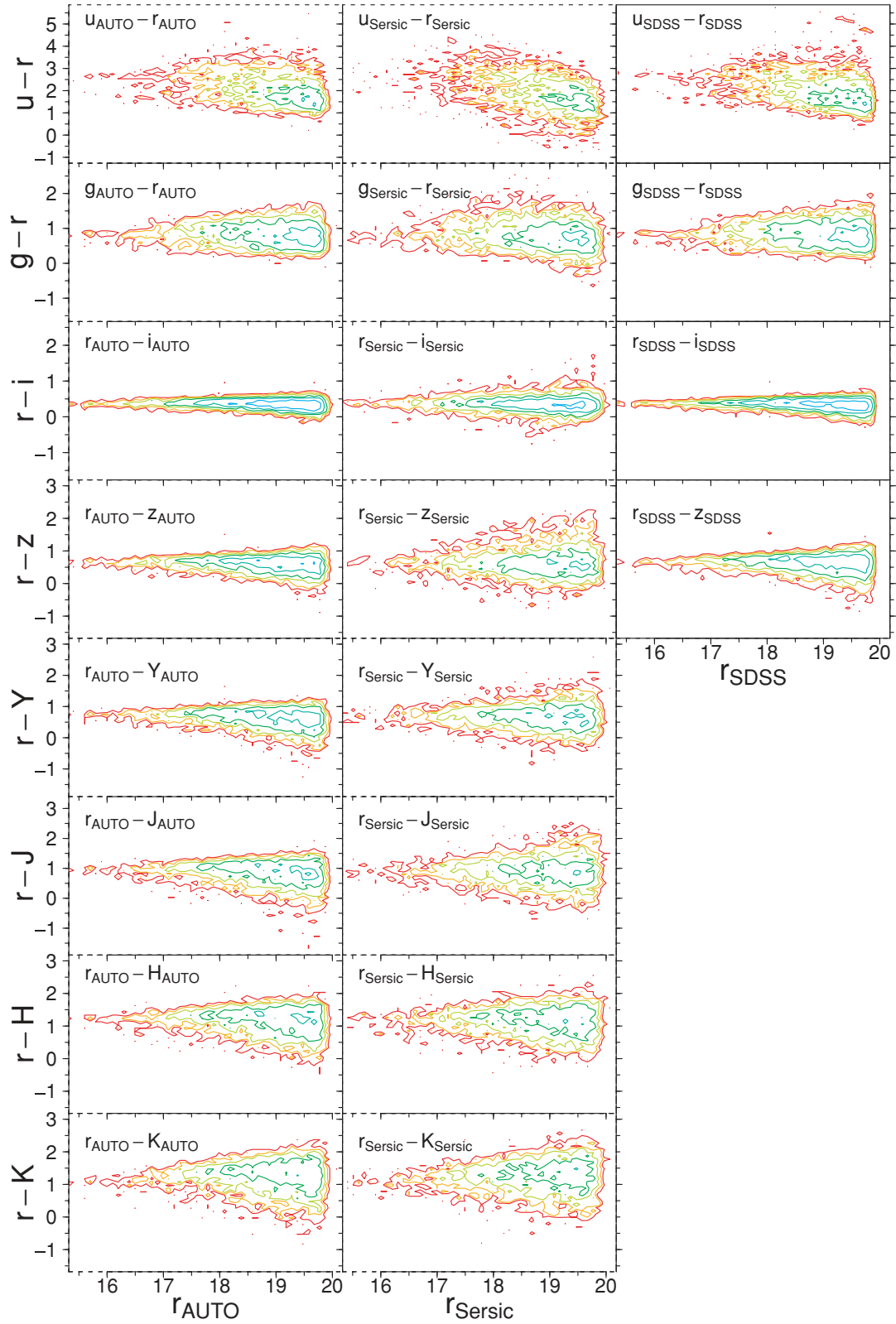


**Figure 20.**  $X - r$  distributions from GAMA  $r$ -band-defined AUTO magnitudes, GAMA Sérsic magnitudes and SDSS PETROMAGS (left-hand to right-hand panel), against  $r$ , for all  $X = u, g, i, z, Y, J, H$  and  $K$ . Sources used are those within the subset region with credible AUTO and Sérsic magnitudes and without the SDSS-saturated object bit set. Contours increase geometrically in powers of 2, from 2 to 512 galaxies  $\text{bin}^{-1}$ . Bins are  $0.1 \text{ mag} \times 0.1 \text{ mag}$  in size.



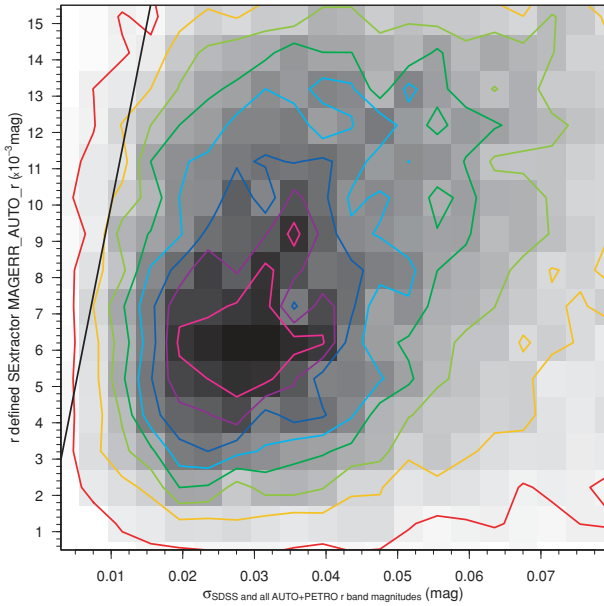


**Figure 21.** The distribution of standard deviation in the  $r$ -band apparent magnitude against SETRACTOR’s calculated magnitude error (using the first quartile gain from the gain distribution of the mosaic’s input images) for our clean sample of galaxies, using SDSS,  $r$ -band-defined,  $K$ -band-defined and self-defined AUTO and PETRO magnitudes to calculate the standard deviation. Contours rise linearly by 16 galaxies  $\text{bin}^{-1}$ , ranging from 8 to 120 galaxies  $\text{bin}^{-1}$ . Bins are 0.004 mag ( $x$ -axis)  $\times$  0.001 mag ( $y$ -axis) in size.

detailed in Sections 3.2 and 3.4 combines images from a number of different stripes to generate the master mosaic. As the mosaics are transformed from different zero-points, the relationship between electrons and pixel counts will be different for each image. This mosaic must suffer from variations in gain. The SETRACTOR utility can be set up to deal with this anomaly, by using the weightmaps generated by SWARP. However, this may introduce a level of surface brightness bias into the resulting catalogue that would be difficult to quantify. We calculate the SETRACTOR magnitude error via the first quartile value, taken from the distribution of gain parameters used to create the mosaic. The gain used in the SDSS calculation is the average for the strip. The SETRACTOR error is calculated using equation (5), where  $A$  is the area of the aperture,  $\sigma$  is the standard deviation in noise and  $F$  is the total flux within the aperture. By using the first quartile gain value, we may be slightly overestimating the  $\frac{F}{\text{gain}}$  component of the magnitude uncertainty calculation. However, given the amount of background noise in the mosaic, this component will constitute only a small fraction towards the error in the fainter galaxies, and in the brighter galaxies, the uncertainty in magnitude due to the aperture definition will be much greater than the SETRACTOR magnitude error itself. The SETRACTOR magnitude error is calculated separately for each aperture type and is available within the GAMA photometric catalogues:

$$\Delta m = \frac{1.0857 \sqrt{A\sigma^2 + \frac{F}{\text{gain}}}}{F}. \quad (5)$$

We have attempted to quantify the uncertainty due to the aperture definition, in order to calculate its extent relative to the SETRACTOR magnitude error. We use the cleaned sample defined in Section 6.1. The dispersion in calculated magnitude between our different photometric methods for this sample is shown in Figs 9–13. Fig. 21 shows the relative scales of the uncertainty due to a galaxy’s aperture definition (calculated from the standard deviation in AUTO/PETRO lumi-

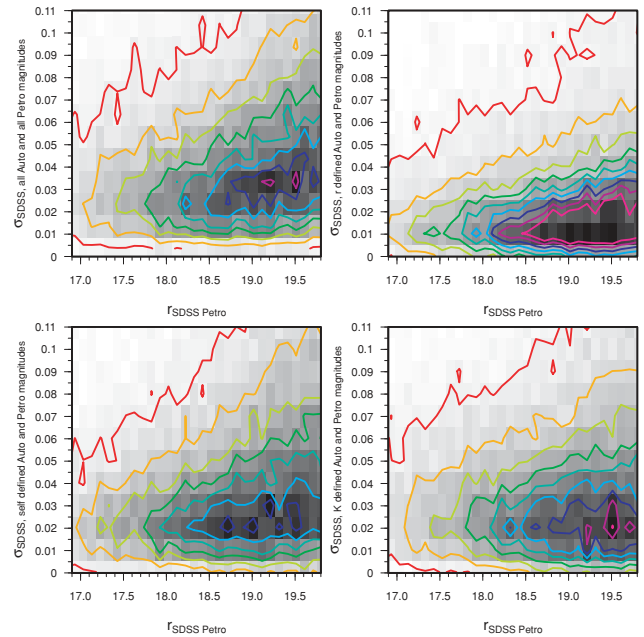


**Figure 22.** The distribution of standard deviation in the  $r$ -band apparent magnitude against apparent magnitude for our clean sample of galaxies, using four different sets of magnitudes to calculate the standard deviation in each case. Contours rise linearly by 20 galaxies  $\text{bin}^{-1}$ , ranging from 10 to 170 galaxies  $\text{bin}^{-1}$ . Bins are 0.1 mag ( $x$ -axis)  $\times$  0.01 mag ( $y$ -axis) in size.

nosities from the SDSS survey and our  $r/K$ /self-defined catalogues) and the error generated by SETRACTOR in the  $r$  band. The aperture definition uncertainty is generally much greater than that due to background variation and signal-to-noise ratio that SETRACTOR derives. Fig. 22 shows how this standard deviation in a galaxy’s  $r$ -band magnitude changes with apparent magnitude. Whilst this uncertainty is larger than the SETRACTOR magnitude error, it is fundamentally a more consistent judgement of the uncertainty in a given galaxy’s brightness as it does not assume that any particular extended-source aperture definition is correct. Whilst the dispersion of the relationship increases with apparent magnitude (along with the number of galaxies), the modal standard deviation is approximately constant. Taking this to be a good estimate of the average uncertainty in the apparent magnitude of a galaxy within our sample, we have confidence in our published apparent magnitudes to within  $\pm 0.03$  mag in  $gri$ ,  $\pm 0.06$  mag in  $z$  and  $\pm 0.20$  mag in  $u$ . We calculate the same statistics in the NIR passbands (though without SDSS PETROMAG). We have confidence in our published apparent magnitudes within  $\pm 0.05$  mag in  $YJHK$ , approximately two and a half times the size of the photometric rms error the UKIDSS was designed to have ( $\pm 0.02$  mag, Lawrence et al. 2007).

## 7.4 Number counts

In order to construct a unbiased data set, it is necessary for us to calculate the apparent magnitude where the GAMA sample ceases to be complete. Table 6 illustrates the size and depth of the GAMA apparent magnitude limited samples. This section describes the definition of these samples.

### 7.4.1 Definition of a GAMA galaxy sample used in this section

The GAMA sample used in this section is defined as those SDSS objects that are within the area that has complete  $ugrizYJHK$  colour

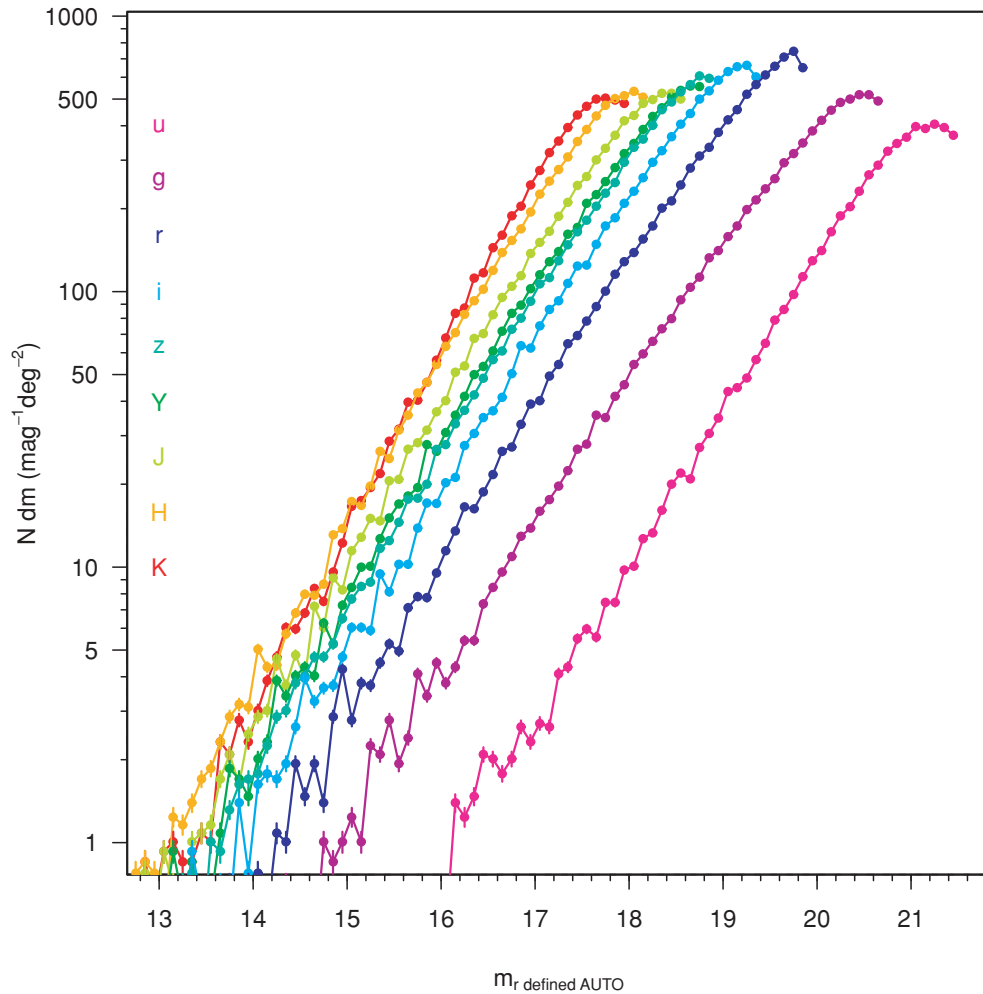


**Figure 23.** Number counts of GAMA galaxies (sources that have passed our star–galaxy separation criteria) with good *ugrizYJHK* colours, split into 0.1-mag bins and divided by the total area they cover. Error bars shown are for Poissonian number counts.

coverage and have passed the star–galaxy separation criteria. Of the 908 022 objects in the GAMA master catalogue, only 124 622 fulfil this criteria. The area of sky that has complete GAMA *ugrizYJHK* coverage is  $129.1232 \pm 0.0008 \text{ deg}^2$ , 89.7 per cent of the entire GAMA region. All magnitudes in this section are *r*-band-defined AUTO magnitudes, unless otherwise defined.

#### 7.4.2 Determination of apparent magnitude limits

Fig. 23 shows how the sky density of GAMA galaxies in the nine passbands varies with apparent magnitude. The distributions peak in the 0.1-mag bins centred at  $u = 21.25$ ,  $g = 20.55$ ,  $r = 19.75$ ,  $i = 19.25$ ,  $z = 18.75$ ,  $Y = 18.65$ ,  $J = 18.45$ ,  $H = 18.05$  and  $K = 17.75$  mag. Tables 7–9 contain the number counts of GAMA galaxies in *ugrizYJHK*, this time using 0.25-mag bins. Poissonian uncertainties are also included. Both sets of data have been converted to  $\text{deg}^{-2} \text{ mag}^{-1}$  units.

The *r*-band number count drop-off, despite hitting the PETROMAG\_R = 19.8 mag GAMA main sample magnitude limit, is not absolute, because the SDSS limit was extended to PETROMAG\_R = 20.5 mag in the GAMA 12 region, so that useful filler objects could be selected, and because radio/*K*/*z*-band-selected objects in G9 and G15 will also be included within the catalogue. Objects that are fainter than  $r_{\text{model}} = 20.5$  mag (722 sources; 0.5 per cent of the

**Table 6.** The number of sources within the star–galaxy separation and apparent magnitude-limited GAMA samples that have a complete set of good *ugrizYJHK* *r*-band-defined magnitudes, the number of those sources that have redshifts from first- and second-year data and the percentage redshift completeness. Apparent magnitudes are *r*-band-defined magnitudes, using the AB magnitude system.

Band	Sources	Redshifts	Per cent redshifts
Star–galaxy separation criteria only	124 622	82 926	66.5
$u \leq 21.0$	46 006	39 767	86.4
$g \leq 20.3$	67 913	58 956	86.8
$r \leq 19.8$	106 032	79 672	75.1
$i \leq 19.0$	74 885	66 981	89.4
$z \leq 18.5$	59 470	55 202	92.8
$Y \leq 18.4$	57 739	53 339	92.4
$J \leq 18.2$	60 213	54 264	90.1
$H \leq 17.8$	55 734	51 033	91.6
$K \leq 17.5$	46 424	43 252	93.2

sample) will be due to differences in object extraction between the SDSS and SExtractor, as mentioned in previous sections.

The turnovers in Fig. 23 will occur where the  $r = 19.8$  mag limit is reached for galaxies with the median passband – *r* colour. We are

**Table 7.** Number counts for the  $ugr$  filters, using  $r$ -band-defined AUTO photometry, with Poissonian uncertainties.

$u$ (mag)	$N_u(m) \pm \sigma_{N_u(m)}$ [deg <sup>-2</sup> (mag) <sup>-1</sup> ]	$g$ (mag)	$N_g(m) \pm \sigma_{N_g(m)}$ [deg <sup>-2</sup> (mag) <sup>-1</sup> ]	$r$ (mag)	$N_r(m) \pm \sigma_{N_r(m)}$ [deg <sup>-2</sup> (mag) <sup>-1</sup> ]
12.125	0.031 ± 0.015	10.125	0 ± 0	10.125	0.031 ± 0.015
12.375	0 ± 0	10.375	0 ± 0	10.375	0 ± 0
12.625	0 ± 0	10.625	0 ± 0	10.625	0 ± 0
12.875	0 ± 0	10.875	0.031 ± 0.015	10.875	0.031 ± 0.015
13.125	0 ± 0	11.125	0 ± 0	11.125	0 ± 0
13.375	0.031 ± 0.015	11.375	0 ± 0	11.375	0.124 ± 0.031
13.625	0.093 ± 0.027	11.625	0.031 ± 0.015	11.625	0.062 ± 0.022
13.875	0.062 ± 0.022	11.875	0 ± 0	11.875	0 ± 0
14.125	0.093 ± 0.027	12.125	0.062 ± 0.022	12.125	0.031 ± 0.015
14.375	0.062 ± 0.022	12.375	0.124 ± 0.031	12.375	0.031 ± 0.015
14.625	0.062 ± 0.022	12.625	0.031 ± 0.015	12.625	0.062 ± 0.022
14.875	0.062 ± 0.022	12.875	0.031 ± 0.015	12.875	0.155 ± 0.035
15.125	0.124 ± 0.031	13.125	0.031 ± 0.015	13.125	0.217 ± 0.041
15.375	0.248 ± 0.044	13.375	0.062 ± 0.022	13.375	0.186 ± 0.038
15.625	0.279 ± 0.046	13.625	0.062 ± 0.022	13.625	0.558 ± 0.066
15.875	0.527 ± 0.064	13.875	0.248 ± 0.044	13.875	0.589 ± 0.068
16.125	0.929 ± 0.085	14.125	0.248 ± 0.044	14.125	0.712 ± 0.074
16.375	1.735 ± 0.116	14.375	0.712 ± 0.074	14.375	1.425 ± 0.105
16.625	1.828 ± 0.119	14.625	0.62 ± 0.069	14.625	1.611 ± 0.112
16.875	2.478 ± 0.139	14.875	0.836 ± 0.08	14.875	3.16 ± 0.156
17.125	3.098 ± 0.155	15.125	1.27 ± 0.099	15.125	3.253 ± 0.159
17.375	4.616 ± 0.189	15.375	2.478 ± 0.139	15.375	4.771 ± 0.192
17.625	6.01 ± 0.216	15.625	2.447 ± 0.138	15.625	6.536 ± 0.225
17.875	8.457 ± 0.256	15.875	4.089 ± 0.178	15.875	8.333 ± 0.254
18.125	11.772 ± 0.302	16.125	4.213 ± 0.181	16.125	13.352 ± 0.322
18.375	17.1 ± 0.364	16.375	6.32 ± 0.221	16.375	17.286 ± 0.366
18.625	22.273 ± 0.415	16.625	9.139 ± 0.266	16.625	24.783 ± 0.438
18.875	31.815 ± 0.496	16.875	13.166 ± 0.319	16.875	34.2 ± 0.515
19.125	44.763 ± 0.589	17.125	16.728 ± 0.36	17.125	46.808 ± 0.602
19.375	58.58 ± 0.674	17.375	24.225 ± 0.433	17.375	64.28 ± 0.706
19.625	84.973 ± 0.811	17.625	31.722 ± 0.496	17.625	85.933 ± 0.816
19.875	117.159 ± 0.953	17.875	42.719 ± 0.575	17.875	118.491 ± 0.958
20.125	159.754 ± 1.112	18.125	58.673 ± 0.674	18.125	151.452 ± 1.083
20.375	211.736 ± 1.281	18.375	74.502 ± 0.76	18.375	200.955 ± 1.248
20.625	282.831 ± 1.48	18.625	101.299 ± 0.886	18.625	271.524 ± 1.45
20.875	351.602 ± 1.65	18.875	132.122 ± 1.012	18.875	347.885 ± 1.641
21.125	396.304 ± 1.752	19.125	170.256 ± 1.148	19.125	454.357 ± 1.876
21.375	386.731 ± 1.731	19.375	222.175 ± 1.312	19.375	575.729 ± 2.112
		19.625	282.428 ± 1.479	19.625	695.832 ± 2.321
		19.875	356.559 ± 1.662	19.875	540.445 ± 2.046
		20.125	446.148 ± 1.859		
		20.375	505.471 ± 1.979		
		20.625	492.894 ± 1.954		

within the domain where the number of galaxies within a magnitude bin increases linearly with increasing apparent magnitude, but a deviation from this relationship is visible in the figure, approximately 3-mag bins before the turnover occurs in all bands except  $r$ . This effect is due to colour incompleteness becoming a factor. Unfortunately, despite our radio/ $K/z$  selection, there will be a population of objects that are bright in other passbands, but too faint in  $r$  to be included within our sample. Assuming the passband –  $r$  colour distribution is approximately Gaussian, this population will feature predominantly in the apparent magnitude bins near the turnover, causing the characteristic flattening we see. Accounting for this effect, we define the apparent magnitude sample limits of our sample to be a few bins brighter than this turnover, where the linear relationship still holds. Our apparent magnitude limits are set to  $u = 21.0$ ,  $g = 20.3$ ,  $r = 19.8$ ,  $i = 19.0$ ,  $z = 18.5$ ,  $Y = 18.4$ ,  $J = 18.2$ ,  $H = 17.8$  and  $K = 17.6$  mag.

### 7.4.3 GAMA apparent-magnitude-limited catalogues

Table 6 contains the sizes of the apparent-magnitude-limited samples and their current redshift completeness. Our magnitude-limited optical samples contain approximately 40 000 less galaxies than the equivalent samples in Blanton et al. (2003), which covers the SDSS DR2 region, but extend 2 mag deeper. When we compare our number counts to 6dFGS (Jones et al. 2009), our samples are also smaller in area coverage, but similar in size and much deeper in magnitude completeness. Hill et al. (2010), our previous attempt at defining a sample across the optical and NIR (combining MGC, SDSS and UKIDSS data to form a  $B$ -band-selected  $ugrizYJHK$  catalogue), was just one-tenth of the size and was 0.2–1.8 mag shallower. Currently, a large fraction of our samples have not been spectroscopically sampled. After the completion of the 2008–09 allocations of AAOmega spectroscopy, our apparent magnitude samples have  $\geq 75$  per cent

**Table 8.** Number counts for the  $izY$  filters, using  $r$ -band-defined AUTO photometry, with Poissonian uncertainties.

$i$ (mag)	$N_i(m) \pm \sigma_{N_i(m)}$ [deg <sup>-2</sup> (mag) <sup>-1</sup> ]	$z$ (mag)	$N_z(m) \pm \sigma_{N_z(m)}$ [deg <sup>-2</sup> (mag) <sup>-1</sup> ]	$Y$ (mag)	$N_Y(m) \pm \sigma_{N_Y(m)}$ [deg <sup>-2</sup> (mag) <sup>-1</sup> ]
9.375	0 ± 0	9.375	0 ± 0	9.375	0.031 ± 0.015
9.625	0 ± 0	9.625	0.031 ± 0.015	9.625	0 ± 0
9.875	0.031 ± 0.015	9.875	0 ± 0	9.875	0.031 ± 0.015
10.125	0 ± 0	10.125	0.031 ± 0.015	10.125	0 ± 0
10.375	0.031 ± 0.015	10.375	0 ± 0	10.375	0 ± 0
10.625	0 ± 0	10.625	0.124 ± 0.031	10.625	0.124 ± 0.031
10.875	0.124 ± 0.031	10.875	0.031 ± 0.015	10.875	0.031 ± 0.015
11.125	0.031 ± 0.015	11.125	0.031 ± 0.015	11.125	0.031 ± 0.015
11.375	0.031 ± 0.015	11.375	0 ± 0	11.375	0 ± 0
11.625	0 ± 0	11.625	0.031 ± 0.015	11.625	0.062 ± 0.022
11.875	0.031 ± 0.015	11.875	0.031 ± 0.015	11.875	0.062 ± 0.022
12.125	0.031 ± 0.015	12.125	0.093 ± 0.027	12.125	0.093 ± 0.027
12.375	0.186 ± 0.038	12.375	0.217 ± 0.041	12.375	0.186 ± 0.038
12.625	0.186 ± 0.038	12.625	0.248 ± 0.044	12.625	0.217 ± 0.041
12.875	0.124 ± 0.031	12.875	0.31 ± 0.049	12.875	0.403 ± 0.056
13.125	0.372 ± 0.054	13.125	0.558 ± 0.066	13.125	0.651 ± 0.071
13.375	0.682 ± 0.073	13.375	0.62 ± 0.069	13.375	0.743 ± 0.076
13.625	0.62 ± 0.069	13.625	1.022 ± 0.089	13.625	1.022 ± 0.089
13.875	0.96 ± 0.086	13.875	1.611 ± 0.112	13.875	1.673 ± 0.114
14.125	1.704 ± 0.115	14.125	1.983 ± 0.124	14.125	2.478 ± 0.139
14.375	2.168 ± 0.13	14.375	3.501 ± 0.165	14.375	3.779 ± 0.171
14.625	3.748 ± 0.17	14.625	4.554 ± 0.188	14.625	4.585 ± 0.188
14.875	3.965 ± 0.175	14.875	5.545 ± 0.207	14.875	6.289 ± 0.221
15.125	5.917 ± 0.214	15.125	8.116 ± 0.251	15.125	9.015 ± 0.264
15.375	8.302 ± 0.254	15.375	11.555 ± 0.299	15.375	13.506 ± 0.323
15.625	10.749 ± 0.289	15.625	16.697 ± 0.36	15.625	17.689 ± 0.37
15.875	16.635 ± 0.359	15.875	21.994 ± 0.413	15.875	25.774 ± 0.447
16.125	22.211 ± 0.415	16.125	32.031 ± 0.498	16.125	34.727 ± 0.519
16.375	31.598 ± 0.495	16.375	43.4 ± 0.58	16.375	49.937 ± 0.622
16.625	40.984 ± 0.563	16.625	61.43 ± 0.69	16.625	69.484 ± 0.734
16.875	60.872 ± 0.687	16.875	83.703 ± 0.805	16.875	93.802 ± 0.852
17.125	82.464 ± 0.799	17.125	113.318 ± 0.937	17.125	124.873 ± 0.983
17.375	111.367 ± 0.929	17.375	151.266 ± 1.082	17.375	161.83 ± 1.12
17.625	142.995 ± 1.052	17.625	198.849 ± 1.241	17.625	221.277 ± 1.309
17.875	193.397 ± 1.224	17.875	264.213 ± 1.43	17.875	292.124 ± 1.504
18.125	253.432 ± 1.401	18.125	356.156 ± 1.661	18.125	375.424 ± 1.705
18.375	336.423 ± 1.614	18.375	458.973 ± 1.885	18.375	480.285 ± 1.929
18.625	438.093 ± 1.842	18.625	561.2 ± 2.085	18.625	549.831 ± 2.064
18.875	549.336 ± 2.063	18.875	582.39 ± 2.124		
19.125	649.457 ± 2.243				
19.375	564.205 ± 2.09				

completeness. It is anticipated that this statistic will rise to  $\geq 95$  per cent after the completion of the 2010 allocation.

### 7.5 Incorporating GALEX data

We have also combined the GAMA sample with UV data. The GAMA master catalogue has been matched to GALEX photometry (Wyder et al. 2005). As GALEX observations are of low resolution (typical imaging FWHM  $\sim 10$  arcsec), the matching is complex compared to the simple UKIDSS/SDSS matching described in this paper as a number of separate SDSS objects may be matched to one larger GALEX object. The precise method of generating the GALEX matches is described in Robotham et al. (in preparation). In summary, all SDSS objects within the 90 per cent Petrosian radius of a GALEX source are considered to be contributing flux to that source. The flux of the GALEX object is then apportioned to

the SDSS objects, with the allotted fraction calculated via the distance between the SDSS and GALEX objects. If no other nearby source is within 2.5 mag (in  $g$ ) of the closest match, then all flux is assigned to the closest match. GALEX has two distinct filters  $NUV$  and  $FUV$ . The generated magnitudes are stored within columns labelled `MAG_AUTO_FUV` and `MAG_AUTO_NUV`.

### 7.6 SED fits using GAMA data

The SEDs of 10 galaxies selected at random from the GAMA sample are shown in Fig. 24. We show the GAMA–GALEX UV luminosities, GAMA total luminosities, Petrosian luminosities taken from the UKIDSS and SDSS surveys, and two Bruzual–Charlot (Bruzual & Charlot 2003) galaxy models with different ages and metallicities. The models are normalized via least-squares best fitting to the nine GAMA data points. For image clarity, we do not show the

**Table 9.** Number counts for the *JHK* filters, using *r*-band-defined AUTO photometry, with Poissonian uncertainties.

<i>J</i> (mag)	$N_J(m) \pm \sigma_{N_J(m)}$ [deg <sup>-2</sup> (mag) <sup>-1</sup> ]	<i>H</i> (mag)	$N_H(m) \pm \sigma_{N_H(m)}$ [deg <sup>-2</sup> (mag) <sup>-1</sup> ]	<i>K</i> (mag)	$N_K(m) \pm \sigma_{N_K(m)}$ [deg <sup>-2</sup> (mag) <sup>-1</sup> ]
9.125	0 ± 0	9.125	0.031 ± 0.015	9.125	0 ± 0
9.375	0 ± 0	9.375	0 ± 0	9.375	0.031 ± 0.015
9.625	0.031 ± 0.015	9.625	0.031 ± 0.015	9.625	0 ± 0
9.875	0.031 ± 0.015	9.875	0 ± 0	9.875	0.031 ± 0.015
10.125	0 ± 0	10.125	0.093 ± 0.027	10.125	0.031 ± 0.015
10.375	0.062 ± 0.022	10.375	0.062 ± 0.022	10.375	0.062 ± 0.022
10.625	0.062 ± 0.022	10.625	0.031 ± 0.015	10.625	0.031 ± 0.015
10.875	0.062 ± 0.022	10.875	0 ± 0	10.875	0.062 ± 0.022
11.125	0 ± 0	11.125	0 ± 0	11.125	0 ± 0
11.375	0 ± 0	11.375	0.031 ± 0.015	11.375	0 ± 0
11.625	0.031 ± 0.015	11.625	0.124 ± 0.031	11.625	0.062 ± 0.022
11.875	0.124 ± 0.031	11.875	0.155 ± 0.035	11.875	0.062 ± 0.022
12.125	0.155 ± 0.035	12.125	0.248 ± 0.044	12.125	0.186 ± 0.038
12.375	0.217 ± 0.041	12.375	0.372 ± 0.054	12.375	0.217 ± 0.041
12.625	0.31 ± 0.049	12.625	0.527 ± 0.064	12.625	0.31 ± 0.049
12.875	0.527 ± 0.064	12.875	0.774 ± 0.077	12.875	0.682 ± 0.073
13.125	0.712 ± 0.074	13.125	0.867 ± 0.082	13.125	0.867 ± 0.082
13.375	0.898 ± 0.083	13.375	1.518 ± 0.108	13.375	1.022 ± 0.089
13.625	1.549 ± 0.11	13.625	2.23 ± 0.131	13.625	1.735 ± 0.116
13.875	2.076 ± 0.127	13.875	3.098 ± 0.155	13.875	2.478 ± 0.139
14.125	3.191 ± 0.157	14.125	4.492 ± 0.187	14.125	3.903 ± 0.174
14.375	4.43 ± 0.185	14.375	6.041 ± 0.216	14.375	5.545 ± 0.207
14.625	5.7 ± 0.21	14.625	7.806 ± 0.246	14.625	7.621 ± 0.243
14.875	8.147 ± 0.251	14.875	12.763 ± 0.314	14.875	10.192 ± 0.281
15.125	12.639 ± 0.313	15.125	17.72 ± 0.37	15.125	17.689 ± 0.37
15.375	17.224 ± 0.365	15.375	24.194 ± 0.433	15.375	23.915 ± 0.43
15.625	24.163 ± 0.433	15.625	35.036 ± 0.521	15.625	35.966 ± 0.528
15.875	33.425 ± 0.509	15.875	49.379 ± 0.618	15.875	49.999 ± 0.622
16.125	46.715 ± 0.601	16.125	70.413 ± 0.738	16.125	77.879 ± 0.777
16.375	66.448 ± 0.717	16.375	94.298 ± 0.855	16.375	109.198 ± 0.92
16.625	92.222 ± 0.845	16.625	133.237 ± 1.016	16.625	158.422 ± 1.108
16.875	121.434 ± 0.97	16.875	176.792 ± 1.17	16.875	218.272 ± 1.3
17.125	162.976 ± 1.123	17.125	245.781 ± 1.38	17.125	305.631 ± 1.538
17.375	220.348 ± 1.306	17.375	319.602 ± 1.573	17.375	406.031 ± 1.773
17.625	288.159 ± 1.494	17.625	420.931 ± 1.806	17.625	488.99 ± 1.946
17.875	384.191 ± 1.725	17.875	504.448 ± 1.977	17.875	491.716 ± 1.951
18.125	464.796 ± 1.897	18.125	515.229 ± 1.998		
18.375	521.394 ± 2.009				

uncertainties on SDSS and UKIDSS data points. GAMA UV uncertainties are taken from SExtractor magnitude errors. GAMA optical and NIR uncertainties are calculated using the standard deviation in the luminosity when different photometric methods are used (following the method described in Section 7.3). In some cases, the photometry provided by survey catalogues and the GAMA photometry are near identical and match the galaxy models well (see 216774 and 137440 on Fig. 24). In other cases, where there is a discrepancy between our derived luminosities and the survey-catalogue parameters, the GAMA photometry is a better fit to the models (e.g. 202588 and 518102 on Fig. 24). We therefore judge our *r*-band-defined AUTO colours to be a significant improvement.

### 7.7 Released GAMA photometry

The GAMA photometry described in this paper provides the GamaPhotom catalogue. This catalogue is filtered and combined with the other GAMA catalogues to produce the first GAMA data release, defined in Driver et al. (2010).

## 8 THE IMPACT OF THE PHOTOMETRIC METHOD ON THE OBSERVED LUMINOSITY DISTRIBUTION

### 8.1 Comparison between *r*-band luminosity functions

In order to illustrate the effect that photometric methods have on statistical measurements of the galaxy population, we derive the *r*-band luminosity function using nine different photometric methods. We use all our photometric systems and the original SDSS photometry, and derive luminosity functions from the same population of galaxies. This should provide a consistent analysis for each method, removing all systematic effects except that produced by the photometric method.

### 8.2 Luminosity distribution and function measurement

A number of techniques exist for measuring the galaxy luminosity distribution (see Willmer 1997) and functions to parametrize it. We follow the methodology described in Hill et al. (2010). This utilizes

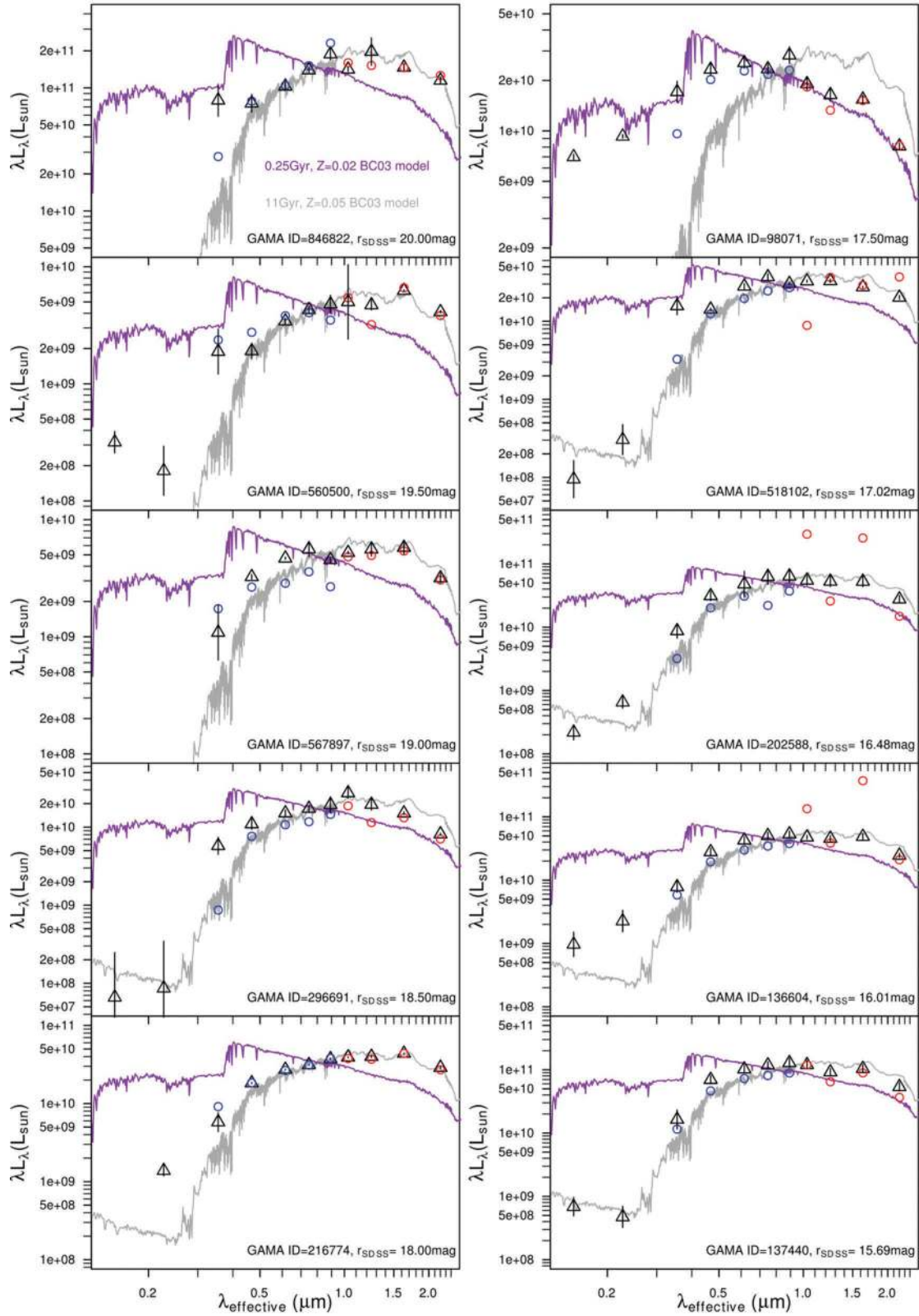


**Figure 24.** SEDs of 10 GAMA galaxies using GAMA-matched GALEX photometry and  $r$ -band-defined AUTO *ugrizYJHK* photometry (black triangles), and the comparable SDSS (blue circles) and UKIDSS (red circles) *PETROMAG* photometry. Uncertainties shown for GAMA *ugrizYJHK* points are calculated from the standard deviation in the photometry (as in Section 7.3). GAMA–GALEX uncertainties are *SExtractor* errors from the GALEX pipeline catalogues. Two Bruzual–Charlot 03 models are also plotted: the grey line is a 11-Gyr model using  $Z = 0.05$  and the purple line is a 0.25-Gyr model using  $Z = 0.02$  ( $Z_{\odot}$ ). The models shown are the same as those in Fig. 16.

**Table 10.** The number of sources that pass our star–galaxy separation criteria, redshift limit and  $r \leq 19.4$  mag limit, depending on which magnitude system is used to define the  $r$ -band magnitude, with comparison luminosity function parameters from the SDSS (Blanton et al. 2003; Montero-Dorta & Prada 2009) and SDSS+MGC (Hill et al. 2010) defined samples. All magnitudes use the AB magnitude system and have been dereddened using the `EXTINCTION_R` SDSS parameter.  $j$  statistics are calculated using  $M_{\odot,r} = 4.71$  from table 1 of Hill et al. (2010). Note that the comparison study samples have much brighter magnitude limits: 17.77 mag in Montero-Dorta & Prada (2009), 17.79 mag in Blanton et al. (2003) and 18.76 mag in Hill et al. (2010).

Magnitude system	Sources	$M^* - 5 \log_{10} h$	$\alpha$	$\phi^* (h^3 \text{Mpc}^{-3})$	$j (\times 10^8 h \text{L}_{\odot} \text{Mpc}^{-3})$
Montero-Dorta & Prada (2009)	–	–20.71	–1.26	0.0093	1.78
Blanton et al. (2003)	–	–20.44	–1.05	0.0149	1.85
Hill et al. (2010)	–	–20.81	–1.18	0.0124	2.29
SDSS PETROMAG	12 599	$-20.612^{+0.031}_{-0.021}$	$-1.076^{+0.013}_{-0.010}$	$0.0130^{+0.0005}_{-0.0003}$	$1.84^{+0.12}_{-0.11}$
SDSS MODEL MAG	12 740	$-20.812^{+0.029}_{-0.023}$	$-1.146^{+0.011}_{-0.009}$	$0.0111^{+0.0004}_{-0.0003}$	$1.99^{+0.13}_{-0.12}$
$r$ -band-defined AUTO	12 292	$-20.789^{+0.035}_{-0.024}$	$-1.111^{+0.015}_{-0.009}$	$0.0114^{+0.0005}_{-0.0003}$	$1.95^{+0.15}_{-0.13}$
$r$ -band-defined PETRO	12 268	$-20.818^{+0.026}_{-0.034}$	$-1.112^{+0.010}_{-0.012}$	$0.0113^{+0.0003}_{-0.0004}$	$1.98^{+0.14}_{-0.13}$
$K$ -band-defined AUTO	10 855	$-20.596^{+0.029}_{-0.031}$	$-1.063^{+0.012}_{-0.013}$	$0.0126^{+0.0004}_{-0.0004}$	$1.74^{+0.12}_{-0.11}$
$K$ -band-defined PETRO	11 265	$-20.699^{+0.034}_{-0.029}$	$-1.087^{+0.013}_{-0.011}$	$0.0123^{+0.0005}_{-0.0004}$	$1.90^{+0.15}_{-0.14}$
Self-defined AUTO	12 284	$-20.734^{+0.033}_{-0.028}$	$-1.097^{+0.013}_{-0.011}$	$0.0119^{+0.0005}_{-0.0004}$	$1.91^{+0.15}_{-0.14}$
Self-defined PETRO	12 247	$-20.781^{+0.031}_{-0.028}$	$-1.100^{+0.012}_{-0.011}$	$0.0117^{+0.0004}_{-0.0004}$	$1.97^{+0.14}_{-0.14}$
Sérsic (TOTAL)	12 711	$-21.142^{+0.038}_{-0.030}$	$-1.203^{+0.011}_{-0.009}$	$0.0090^{+0.0004}_{-0.0003}$	$2.30^{+0.19}_{-0.18}$

the stepwise maximum-likelihood method (SWML), originally described in detail in Efstathiou, Ellis & Peterson (1988), and the standard functional form, the Schechter luminosity function (Schechter 1976). In Hill et al. (2010), we developed a unique flux limit for each object based upon the spectroscopic limit and a colour limit. As we are working only in the  $r$  band, the colour limit is now used to calculate the change in the magnitude limit between the studied photometric method and SDSS PETROMAG. We now set the apparent magnitude threshold for each object using  $r_{\text{aperture,limit}} = 19.4$  mag. An unfortunate side-effect of the SWML method is that it requires normalization to calculate the luminosity density. We use the method of luminosity density scaling described in sections 3.1.2 and 3.1.4 of Hill et al. (2010). This involves calculating the number density of galaxies within a 1 mag range containing the  $M^*$  mag galaxies and using this to work out the required scaling multiplier. We also account for the cosmic variance within the GAMA regions. We calculate the source density of galaxies within a 5150-deg<sup>2</sup> section of the SDSS survey (large enough for cosmic variance to be negligible) with dereddened  $-21.09 < M_r - 5 \log_{10} h < -20.09$  (i.e.  $M^* - 5 \log_{10} h \pm 0.5$  mag, taking  $M^* - 5 \log_{10} h$  from the  $r$ -band-defined  $r_{\text{AUTO}}$  photometry) and  $0.023 < z < 0.1$ , and compare this with the source density calculated (using the same catalogue) from the GAMA regions of sky. We find that the GAMA regions are 95.2 per cent as dense as the SDSS superpopulation<sup>5</sup> and therefore scale our  $\phi^*$  parameters upwards by a factor of  $\frac{1}{0.952}$ . The area incompleteness of the  $K$ -band-defined sample is accounted for by calculating the normalization volume with area = 133.5 deg<sup>2</sup> (the total coverage of the GAMA regions by  $K$ -band UKIDSS data), rather than the area = 143.9 deg<sup>2</sup> used for the other samples.

<sup>5</sup> In essence, the GAMA survey is a post-stratified sampling of the SDSS, with the GAMA regions a stratum of the entire SDSS area. The SDSS source density is a universal parameter of our superpopulation and can be used to improve the accuracy of the total luminosity density estimation we make from the GAMA data set.

### 8.3 Sample selection

We limit our sample using our star–galaxy separation criteria and an apparent magnitude limit of  $r \leq 19.4$  mag (imposed on the dereddened magnitude system used to calculate the luminosity function). We use a brighter apparent magnitude cut than that defined in Section 7.4, because 19.4 mag is the GAMA sample’s target completeness limit over all three regions. Brighter than this limit, our samples are 91.3 per cent spectroscopically complete (using  $r_{\text{AUTO}}$ ). Our samples suffer greatly from spectroscopic incompleteness fainter than this magnitude limit. We impose a limit based on the spectroscopic limit and a colour limit [i.e.  $19.4 - (r_{\text{SDSS}} - r_{\text{aperture}})$ ]. To remove the necessity of modelling the  $K$  or  $E$  corrections for each galaxy, we also impose a redshift limit of  $0.0033 < z \leq 0.1$ . We adopt an evolution  $\beta = 0$  [where  $E(z) = 2.5\beta \log_{10}(1+z)$ , setting  $\beta = 0$  denotes no evolution in this redshift range] and  $K(z) = 0.95z$  (following the  $r$  band in Hill et al. 2010). We use the SDSS `EXTINCTION_R` parameter to deredden all our photometric methods. We combine the data from the three GAMA regions and treat them as one sample. Column 2 of Table 10 contains our sample sizes.

### 8.4 The effects of surface brightness bias on the presented luminosity distributions

Aperture selection can systematically bias the calculation of the luminosity distribution, particularly where a sample has a high surface brightness constraint (see Cross & Driver 2002, particularly their fig. 5, and Cameron & Driver 2007). The SDSS photometric pipeline unfortunately is incomplete for  $\mu_{r,50} > 23$  mag arcsec<sup>-2</sup> (see section 3.4 of Baldry et al. 2010 and references therein). It follows that any spectroscopic survey that bases itself upon SDSS photometry, such as GAMA, will suffer from the same flaw. Cross & Driver (2002) have quantified the surface brightness dependency that the luminosity distribution inherently suffers from and advise that a bivariate brightness distribution is the best way to quantify, and remove, surface brightness bias. That is beyond the scope of this paper, but this shall be explored in subsequent work. Cross & Driver (2002)

point out that a sample that is complete to  $\mu_{\text{lim}} \geq 24 \text{ mag arcsec}^{-2}$  has very little uncertainty in its Schechter parameters due to surface brightness selection effects, as the  $L^*$  population that define the fitting are fully covered (see also section 4.1.2 of Driver et al. 2005). VST KIDS should provide such a catalogue. For now, however, we accept that the SDSS input catalogue will not contain all faint, low surface brightness galaxies. The luminosity functions we present in this section are for samples that are surface brightness complete to  $\mu_{r,50} < 23 \text{ mag arcsec}^{-2}$  and suffer from varying levels of completeness between  $23 < \mu_{r,50} < 26 \text{ mag arcsec}^{-2}$ . Although these luminosity functions are for a specifically low redshift sample, however, the effects of the surface brightness selection bias should be minimized.

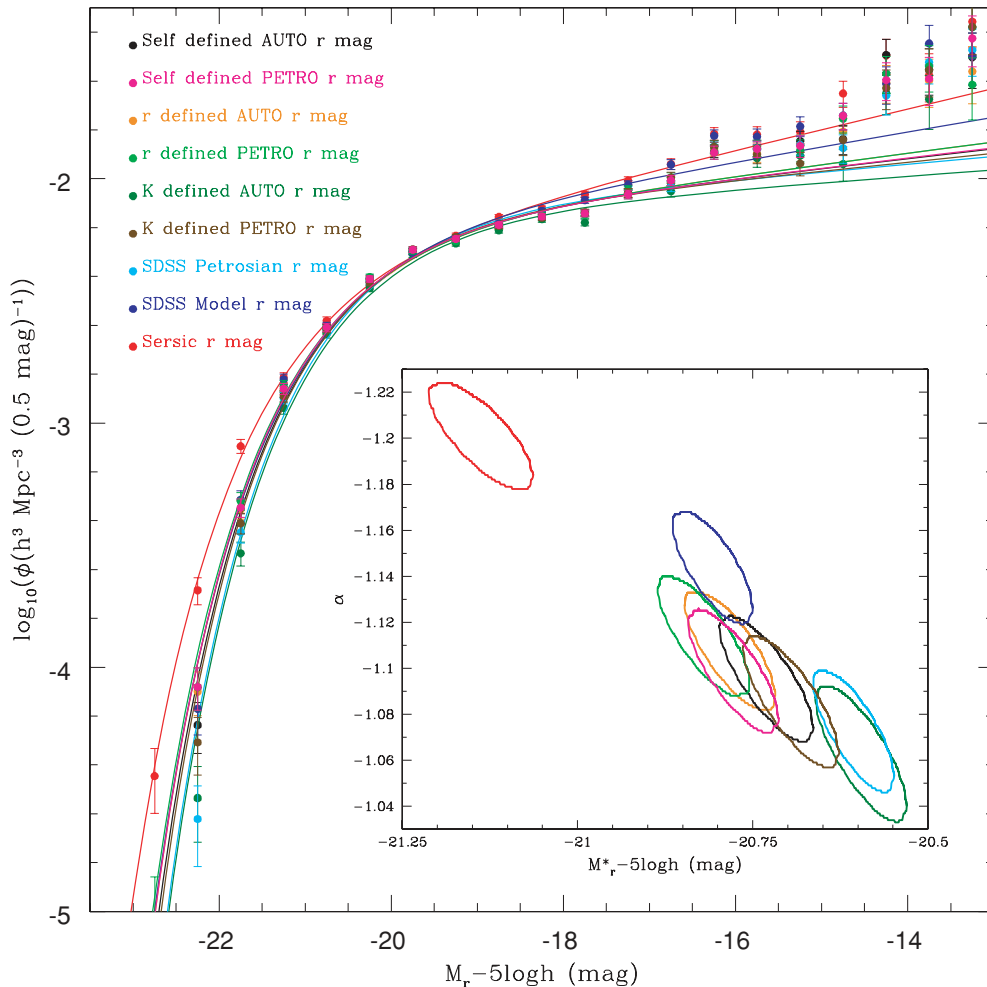
### 8.5 The effects of the aperture definition system on output Schechter parameters

Fig. 25 shows the luminosity distributions generated from different aperture systems and illustrates how dependent the best-fitting luminosity function parameters are on the choice of aperture definition. The best-fitting Schechter function parameters (calculated via  $\chi^2$  minimization) are shown in Table 10.

The proximity of the  $r$ -band- and self-defined magnitude luminosity distributions signifies that changing the SExtractor de-

tection threshold (these catalogues utilize a detection threshold of  $1.7$  and  $1\sigma$ , respectively) has a limited effect on the properties of a large sample ( $M^* - 5 \log_{10} h \pm 0.055 \text{ mag}$ ,  $\alpha \pm 0.014$ ,  $\phi^* \pm 0.0005 h^3 \text{ Mpc}^{-3}$ ). There is an offset between the  $K$ -band and  $r$ -band-defined best-fitting luminosity functions. This is not caused by the cosmic variance in the missing area of the  $K$ -band sample; the best-fitting Schechter function parameters vary only slightly when this is accounted for. By using the COVER\_BITWISE flag, we can define a population of galaxies that are covered by  $K$ -band imaging. The best-fitting Schechter parameters for an  $r_{\text{AUTO}}$  sample within an area covered by  $K$ -band imaging (and normalized to the smaller volume) are  $M^* - 5 \log_{10} h = -20.791 \text{ mag}$ ,  $\alpha = -1.115$  and  $\phi^* = 0.0114 h^3 \text{ Mpc}^{-3}$  – consistent with the area-complete luminosity function within the uncertainty. It may be caused by a systematic alteration in the definition of the apertures used to calculate the flux of the galaxy population.

The best-fitting elliptical Kron and Petrosian aperture luminosity functions are similarly distributed in the  $r$ -,  $K$ - and self-defined samples, indicating that the choice of light-distribution-defined aperture does produce an offset that can be quantified. Whether the aperture is circular or elliptical is important. The SDSS PETROMAG luminosity distribution should be similar to the  $r$ -band and self-defined elliptical PETRO distributions, but there is a notable  $M^* - 5 \log_{10} h$  offset ( $0.20 \text{ mag}$ ; inset of Fig. 25). There is also a marked



**Figure 25.** Luminosity distributions, and the best-fitting Schechter functions, calculated using different aperture definitions. Inset:  $1\sigma$  chi-squared best-fitting contours in the  $M^* - \alpha$  plane. Errors on luminosity distribution points are Poissonian errors.



discrepancy between luminosity distributions calculated using total magnitude apertures (Sérsic and SDSS MODELMAG) and light-distribution-defined apertures. The luminosity distributions of the former are overdense for faint galaxies ( $M_r - 5 \log_{10} h \geq -16$ ) and their best-fitting power-law slopes are thus flatter.

The Sérsic luminosity distribution also measures higher densities of the brightest galaxies. This result is real; we have visually inspected the 139 galaxies that are distributed in the  $-22 \leq M_r - 5 \log_{10} h \leq -21.5$  magnitude bin and only two have suffered catastrophic failures.<sup>6</sup> The remainder are generally well fitted, though prominent spiral features do pose difficulties for the fitting algorithm. Of the 527 galaxies with  $M_{r,\text{Sérsic}} - 5 \log_{10} h < -21$  mag within our redshift-limited, apparent magnitude cut sample, only eight have  $m_{r,\text{SDSS}} - m_{r,\text{Sérsic}} > 0$ . The marked discrepancy between the Sérsic  $M^* - 5 \log_{10} h$  parameter and that generated with the other samples (0.33 mag brighter) is indicative of a scenario where galaxies are moved out of the magnitude bins near  $M^* - 5 \log_{10} h$  and into the brighter bins.  $M^*$  is not an independent parameter; it is correlated with the other Schechter parameters and accordingly the  $\phi^*$  parameter has declined. The total luminosity density ( $j$  in Table 10), whilst 15 per cent higher, is consistent with that generated by the SDSS model magnitude within uncertainties. As our Sérsic magnitudes are not truncated, and the SDSS model magnitudes are truncated at  $7R_e$  for a de Vaucouleurs profile and  $3R_e$  for an elliptical profile, the  $M^*$  offset between these photometric systems is expected. We note that the residuals generated by this Sérsic-fitting process expose the requirement of multicomponent galaxy decomposition; many galaxies have some structure within their central bulges that the Sérsic pipeline cannot model. A multicomponent extension to this pipeline is detailed in Kelvin et al. (2010) and that paper also examines any discrepancies between the Sérsic and multiple-component fitting results. No matter which aperture system we use, the luminosity distribution is overdense in the  $M_r - 5 \log_{10} h > -16$  magnitude bins when compared to the best-fitting luminosity function. This indicates an upturn in the space density of galaxies at the dwarf-giant boundary and the limitations of the single Schechter function fit.

As noted in the Introduction, the Schechter parameters generated are for a sample that will suffer surface brightness incompleteness fainter than  $\mu = 23$  mag arcsec<sup>-2</sup>. In a future paper, we intend to account for this effect by undertaking a complete bivariate brightness analysis of the sample. The total luminosity densities we show here may therefore be systematically underdense due to surface brightness limitations (cf. Cross & Driver 2002). It is also apparent that the simple Schechter function parametrization is no longer a good fit for the luminosity distribution of galaxies at fainter magnitudes; there is an obvious upturn in each sample that is not being modelled. As the Sérsic photometric system is the only system that accounts for missing light, it is the most effective way of calculating the luminosity distribution.

## 9 SUMMARY

The GAMA photometric pipeline has been designed to combine photometric data from a number of sources in a scientific and consistent manner. We have generated a series of large mosaics from imaging data taken from the SDSS and UKIDSS instruments using the SWARP utility and undertaken optical and NIR photometry on an

$r$ - and  $K$ -band-defined sample of sources using SExtractor. We have also used a GALFIT-based pipeline (SIGMA) to generate Sérsic *ugrizYJHK* magnitudes for all sources within the GAMA sample that pass our star-galaxy separation criteria.

We have created a set of  $r$ -band-defined source catalogues in the *ugrizYJHK* passbands, calculated the apparent magnitude limits at which these samples are complete and estimated their current redshift completeness. Whilst these samples do not contain as many sources as those used to calculate the SDSS luminosity functions (Blanton et al. 2003; Montero-Dorta & Prada 2009), they are complete to a greater depth. Our NIR apparent-magnitude-limited catalogues are of comparable size to those produced by the 6dFGS (Jones et al. 2009), with the decrease in coverage area matched by increasing depth. Our source catalogues have the advantage that they can be used to accurately compare the optical and NIR luminosity of any source within our sample. As the aperture definition is constant, we can calculate exact colours. We have attempted to quantify the level of uncertainty in source flux due to the definition of the aperture. We find that the uncertainty is generally  $\sim 400$  per cent of the SExtractor output uncertainty (produced by background noise variations and signal-to-noise ratio).

We have attempted to quantify the percentage of mismatches between our catalogues and the SDSS catalogues. We have taken a subset region of our images and tested their results against the SDSS detection software. We have detailed reasons for mismatches between these catalogues. They are generally an issue of different deblending decisions, artefacts, background noise or proximity to saturated stars. We find that there do seem to be some low surface brightness, compact objects that are missed by the SDSS detection software and are found by SExtractor, and some false SDSS detections. These faulty sources would be removed from the spectroscopic observing list by the extensive visual classification process undertaken by the GAMA team.

As our Sérsic magnitudes are generated from the images that the profile is calculated on, the colours produced from the Sérsic magnitudes are liable to be inaccurate and suffer from bias due to the aperture definition. We have defined a set of ‘fixed-aperture’ Sérsic magnitudes using the Sérsic  $r$ -band magnitude and colours from the  $r$ -band-defined AUTO catalogue. We recommend the use of these magnitudes, called  $X_{\text{total}}$ . These magnitudes will provide both an accurate estimate of the luminosity of each galaxy and optimal colours.

The GAMA photometric pipeline catalogue does not have the breadth of focus that the existing products from the SDSS and UKIDSS surveys have. As both the instrument gain (in SDSS only) and seeing change from frame to frame, our mosaics have variations within them that would cause errors in the calculation of stellar photometry. We have not attempted to deal with saturated objects, which causes uncertainty at the bright end of our catalogue, or masking of artefacts. These problems primarily affect stars and are removed following the extensive visual classification programme we have undertaken. For the task our catalogues were developed, the accurate calculation of extended source apertures across instruments for a specific sample of extended sources, they are more adept than the existing tools.

Finally, we have generated  $r$ -band luminosity distributions and best-fitting luminosity functions from our population of galaxies using nine different aperture definitions: SDSS circular Petrosian and Model magnitudes,  $r$ -band-defined elliptical Petrosian and AUTO magnitudes,  $K$ -band-defined elliptical Petrosian and AUTO magnitudes, self-defined elliptical Petrosian and AUTO magnitudes, and an elliptical Sérsic total magnitude. We find that the  $r$ -band and

<sup>6</sup> These profiles are viewable at <http://star-www.st-and.ac.uk/~dth4/139eye/>

self-defined elliptical, light-distribution-defined apertures produce similar results, indicating that the choice of detection threshold is unimportant. We find that there is a similar AUTO–PETRO offset in the  $r$ -band, self- and  $K$ -band-defined samples. We find that the use of circular apertures does have an effect on the best-fitting Schechter fit, with the SDSS PETROMAG having a fainter  $M^*$  parameter than the SExtractor samples. We also find that the use of total magnitude systems affects the slope of the luminosity function, with both the Sérsic and SDSS MODEL MAG luminosity functions having a steeper  $\alpha$  parameter. When we calculate the total luminosity density for each sample, we find that using the Sérsic magnitude system gives us a higher value, approximately 15 per cent higher than samples that use other aperture definition systems. Following visual classification of a subsection of our sample, it is clear that this is not due to errors within our Sérsic magnitude calculation. We also note that the Schechter luminosity function does not provide a good fit at the faint end of the luminosity distribution and a clear upturn at the dwarf-giant boundary is seen.

## ACKNOWLEDGMENTS

DTH and LSK are funded by STFC studentships. ASGR is funded by a STFC grant. AMH acknowledges support provided by the Australian Research Council through a QEII Fellowship (DP0557850).

Funding for the SDSS and SDSS-II has been provided by the Alfred P. Sloan Foundation, the Participating Institutions, the National Science Foundation, the US Department of Energy, the National Aeronautics and Space Administration, the Japanese Monbukagakusho, the Max Planck Society, and the Higher Education Funding Council for England. The SDSS website is <http://www.sdss.org/>. The SDSS is managed by the Astrophysical Research Consortium for the Participating Institutions. The Participating Institutions are the American Museum of Natural History, Astrophysical Institute Potsdam, University of Basel, University of Cambridge, Case Western Reserve University, University of Chicago, Drexel University, Fermilab, the Institute for Advanced Study, the Japan Participation Group, Johns Hopkins University, the Joint Institute for Nuclear Astrophysics, the Kavli Institute for Particle Astrophysics and Cosmology, the Korean Scientist Group, the Chinese Academy of Sciences (LAMOST), Los Alamos National Laboratory, the Max-Planck-Institute for Astronomy (MPIA), the Max-Planck-Institute for Astrophysics (MPA), New Mexico State University, Ohio State University, University of Pittsburgh, University of Portsmouth, Princeton University, the United States Naval Observatory, and the University of Washington.

The UKIDSS project is defined in Lawrence et al. (2007). The UKIDSS uses the UKIRT Wide Field Camera (WFCAM; Casali et al. 2007) and a photometric system described in Hewett et al. (2006). The pipeline processing and science archive are described in Irwin et al (in preparation) and Hambly et al. (2008).

STILTS is a set of command-line-based catalogue matching tools, based upon the STIL library. It is currently being supported by its author (Mark Taylor) and can be downloaded from <http://www.star.bris.ac.uk/~mbt/stilts/>.

We thank Robert Lupton for his useful comments and suggestions when refereeing this paper.

## REFERENCES

Abazajian K. et al., 2004, *AJ*, 128, 502  
 Adelman-McCarthy J. K. et al., 2008, *ApJS*, 175, 297  
 Andreon S., 2002, *A&A*, 382, 495

Baldry I. K. et al., 2010, *MNRAS*, 404, 86  
 Bertin E., Arnouts S., 1996, *A&AS*, 117, 393  
 Bertin E., Mellier Y., Radovich M., Missonnier G., Didelon P., Morin B., 2002, in Bohlender D. A., Durand D., Handley T. H., eds, *ASP Conf. Ser. Vol. 281, Astronomical Data Analysis Software and Systems XI, The TERAPIX Pipeline*. Astron. Soc. Pac., San Francisco, p. 228  
 Blanton M. R. et al., 2003, *ApJ*, 592, 819  
 Brown R. J. N. et al., 2003, *MNRAS*, 341, 747  
 Bruzual G., Charlot S., 2003, *MNRAS*, 344, 1000  
 Cameron E., Driver S. P., 2007, *MNRAS*, 377, 523  
 Caon N., Capaccioli M., Rampazzo R., 1990, *A&AS*, 86, 429  
 Casali M. et al., 2007, *A&A*, 467, 777  
 Chabrier G., 2003, *PASP*, 115, 763  
 Cohen M., Wheaton W. A., Megeath S. T., 2003, *AJ*, 126, 1090  
 Cross N., Driver S. P., 2002, *MNRAS*, 329, 579  
 de Vaucouleurs G., 1948, *Ann. Astrophys.*, 11, 247  
 Driver S. P., Liske J., Cross N. J. G., De Propris R., Allen P. D., 2005, *MNRAS*, 360, 81  
 Driver S. P. et al., 2009, *Astron. Geophys.*, 50, 050000  
 Driver S. P. et al., 2010, preprint (arXiv:1009.0614)  
 Eales S. et al., 2010, *PASP*, 122, 499  
 Efsthathiou G., Ellis R. S., Peterson B. A., 1988, *MNRAS*, 232, 431  
 Freeman K. C., 1970, *ApJ*, 160, 811  
 Graham A. W., 2001, *AJ*, 121, 820  
 Graham A. W., Driver S. P., 2005, *PASA*, 22, 118  
 Graham A. W., Driver S. P., Petrosian V., Conselice C. J., Bershadsky M. A., Crawford S. M., Goto T., 2005, *AJ*, 130, 1535  
 Hambly N. C. et al., 2008, *MNRAS*, 384, 637  
 Hewett P. C., Warren S. J., Leggett S. K., Hodgkin S. T., 2006, *MNRAS*, 367, 454  
 Hill D. T., Driver S. P., Cameron E., Cross N., Liske J., Robotham A., 2010, *MNRAS*, 404, 1215  
 Høg E. et al., 2000, *A&A*, 355, L27  
 Ivezić Ž et al., 2004, *Astron. Nachr.*, 325, 583  
 Jones D. H. et al., 2009, *MNRAS*, 399, 683  
 Kelvin L., Driver S., Robotham A., Hill D., Cameron E., 2010, in Debattista V. P., Popescu C. C., eds., *AIP Conf. Ser. Vol. 1240, Exploring Galaxy Formation and Evolution via Structural Decomposition*. Am. Inst. Phys., New York, p. 247  
 Kron R. G., 1980, *ApJS*, 43, 305  
 Lawrence A. et al., 2007, *MNRAS*, 379, 1599  
 Montero-Dorta A. D., Prada F., 2009, *MNRAS*, 399, 1106  
 Patterson F. S., 1940, *Harvard College Obser. Bull.*, 914, 9  
 Peng C. Y., Ho L. C., Impey C. D., Rix H. W., 2007, *BAAS*, 38, 804  
 Petrosian V., 1976, *ApJ*, 209, L1  
 Pier J. R. et al., 2003, *AJ*, 125, 1559  
 Robotham A. et al., 2010, *PASA*, 27, 76  
 Schechter P., 1976, *ApJ*, 203, 297  
 Sérsic J. L., 1963, *Bol. Asoc. Argentina de Astron. La Plata Argentina*, 6, 41  
 Smith A. J., Loveday J., Cross N. J. G., 2009, *MNRAS*, 397, 868  
 Stoughton C. et al., 2002, *AJ*, 123, 485  
 Strauss M. A. et al., 2002, *AJ*, 124, 1810  
 Taylor M. B., 2006, in Gabriel C., Arviset C., Ponz D., Enrique S., eds, *ASP Conf. Ser. Vol. 351, STILTS - A Package for Command-Line Processing of Tabular Data*. Astron. Soc. Pac., San Francisco, p. 666  
 Warren S. J. et al., 2007, *MNRAS*, 375, 213  
 Willmer C. N. A., 1997, *AJ*, 114, 898  
 Wyder T. K. et al., 2005, *ApJ*, 619, L15  
 York D. G. et al., 2000, *AJ*, 120, 1579  
 Zacharias N. et al., 2000, *AJ*, 120, 2131

## APPENDIX A: VARIATION BETWEEN PASSBANDS

Fig. A1 shows the 18 200 × 200 pixel images of the piece of sky containing SDSS object 588848900968480848, nine cut-outs from

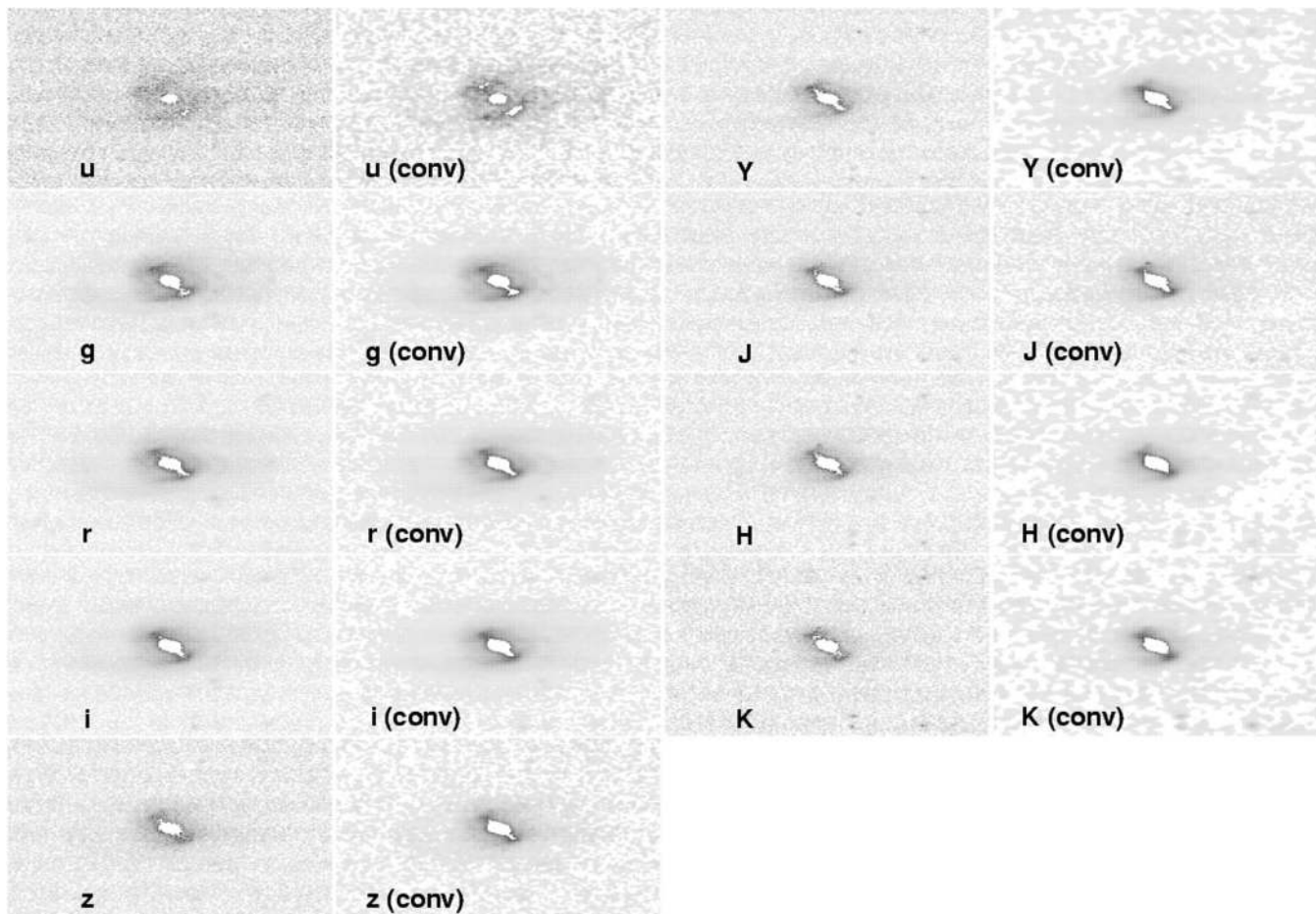


**Figure A1.** The effects of convolution and the change in passband of observations of SDSS object 588848900968480848.

the standard image mosaics and nine from the convolved image mosaics. What is easily notable is that not only does the ability to see features of the object changes dramatically between the  $u$  (top left-hand panel) and  $K$  (bottom right-hand panel) wavebands (spiral arms are visible in the optical, but in the  $K$  band, there only seems to be a bar and a bulge component), but also objects around it appear and disappear (a small blip to the south-east in the  $r$  band that may or may not be part of the object itself, at least five faint objects to the east of the frame in the NIR). The size of the object seems to halve from the  $g$  band to the  $J$  band, though this may be an effect of the image quality (the SDSS  $g$  band should have a much smoother background than the UKIDSS  $J$ ). The apparent magnitude of the object itself changes by 2.8 mag from  $u$  to its peak in  $H$  (SEXTRACTOR calculates AB magnitudes using an  $r$ -band-

defined AUTO aperture of 16.67, 15.44, 14.85, 14.49, 14.32, 14.23, 14.04, 13.83 and 14.11 mag in  $ugrizYJHK$ ). This is probably due to the decrease in dust opacity from the UV to the NIR.

The convolved images also show greater variation between the object and the background (these images all use a linear scale between the 99.5 per cent quantile pixel and 0, the background). For instance, the extended spiral arm to the left-hand side of the bulge in the  $u$  band becomes slightly more apparent in the convolved  $u$ -band image. The size of the object in the convolved images generally looks larger than the standard images, though this again is probably due to the smoothing of the background, making flux overdensities more apparent in the convolved images.

This paper has been typeset from a  $\text{\TeX}/\text{\LaTeX}$  file prepared by the author.